# From Chromospheric Evaporation to Coronal Rain: An Investigation of the Mass and Energy Cycle of a Flare

Seray Şahin[1] and Patrick Antolin[1]

[1]*Department of Mathematics, Physics and Electrical Engineering, Northumbria University, Newcastle Upon Tyne, NE1 8ST, UK*

## ABSTRACT

Chromospheric evaporation (CE) and coronal rain (CR) represent two crucial phenomena encompassing the circulation of mass and energy during solar flares. While CE marks the start of the hot inflow into the flaring loop, CR marks the end, indicating the outflow in the form of cool and dense condensations. With *IRIS* and *AIA/SDO*, we examine and compare the evolution, dynamics, morphology, and energetics of the CR and CE during a C2.1 flare. The CE is directly observed in imaging and spectra in the Fe XXI line with *IRIS* and in the Fe XVIII line of AIA, with upward average total speeds of $138 \pm [35]$ km s$^{-1}$ and a temperature of $[9.03 \pm 3.28] \times 10^6$ K. An explosive to gentle CE transition is observed, with an apparent reduction in turbulence. From quiescent to gradual flare phase, the amount and density of CR increases by a factor of $\approx 4.4$ and 6, respectively. The rain's velocity increases by a 1.4, in agreement with gas pressure drag. In contrast, the clump widths variation is negligible. The location and morphology of CE match closely those of the rain showers, with similar CE sub-structure to the rain strands, reflecting fundamental scales of mass and energy transport. We obtain a CR outflow mass three times larger than the CE inflow mass, suggesting the presence of unresolved CE, perhaps at higher temperatures. The CR energy corresponds to half that of the CE. These results suggest an essential role of coronal rain in the mass-energy cycle of a flare.

*Keywords:* Coronal rain; Solar prominences (1519); Solar chromosphere (1479); Solar transition region (1532); Solar coronal heating (1989), chromospheric evaporation, mass-energy cycle

## 1. INTRODUCTION

Solar flares are one of the most fascinating and, at the same time, the most energetic phenomena in the universe that can be spatially and temporally resolved. These events involve the reconfiguration of the magnetic field, which is known as magnetic reconnection (e.g., Sweet 1958; Shibata & Magara 2011). During this reconnection, a solar flare suddenly releases energy ($10^{28}$-$10^{32}$ erg) stored in the magnetic field (Fletcher et al. 2011) within a typical timescale of tens of minutes. Solar flares have three distinct phases (Golub & Pasachoff 2009) in their temporal evolution known as pre-flare (or precursor), impulsive, and gradual phases. In the pre-flare phase, a series of small brightenings occur before the onset of a flare, playing a crucial role as early indicators of a flare trigger. These triggers encompass various phenomena, such as the emergence of new flux or activation of filaments. As the system undergoes destabilization, the interaction between magnetic fluxes occurs, primarily through reconnection, releasing large amounts of free magnetic energy and subsequently initiating the flare and starting the impulsive phase. This results in the visibility of coronal plasma in soft X-ray and extreme ultraviolet (EUV) lines. During the impulsive phase, a substantial acceleration of electron and ion beams and a reconfiguration of the magnetic field also occur. The energy released through magnetic field dissipation and accelerated particles is readily observed in flare lightcurves derived from various sources, including hard and soft X-rays (HXR and SXR, respectively), $\gamma$-rays, EUV, and, in certain instances, white light emission (Fletcher et al. 2011). The accelerated electron beams propagate downward along the loop legs and heat

Corresponding author: Seray Şahin
seraysahin93@gmail.com

the chromospheric plasma rapidly. At the same time, the reconfigured magnetic field following reconnection does work through the Lorentz force on the plasma, and magnetic energy is converted to kinetic energy in the loops. Energy is transported downwards through thermal conduction, thereby also heating the chromosphere. The increase of temperature in the chromosphere increases the pressure, which drives the chromospheric material upward, filling up the flare loop in a process commonly known as chromospheric evaporation (CE) (Fisher et al. 1985; Dudík et al. 2016). The onset of chromospheric evaporation is marked by the appearance of flare ribbons in chromospheric lines (like Hα). Following the impulsive phase, the gradual phase of a solar flare ensues, spanning several hours or even extending to a day or longer. This phase is characterized by cooling processes and a decline in the intensity of X-ray and EUV emissions. The cooling process within this phase can be further divided into three distinct stages (Scullion et al. 2016). Thermal conduction is initially the primary loss mechanism, driven by elevated temperatures. As the temperature gradually decreases, radiative cooling becomes more effective, aided by the increasing radiative loss function at lower temperatures (Culhane et al. 1970). Ultimately, thermal instability (TI) is thought to set in, accelerating the cooling and producing dense and cool condensations radiating strongly in chromospheric lines that subsequently fall down as coronal rain. The flare loop is thought to largely evacuate and return to thermal equilibrium. Flare-driven coronal rain seems to be present in most flares (Mason et al. 2019), but a large-scale statistical investigation awaits.
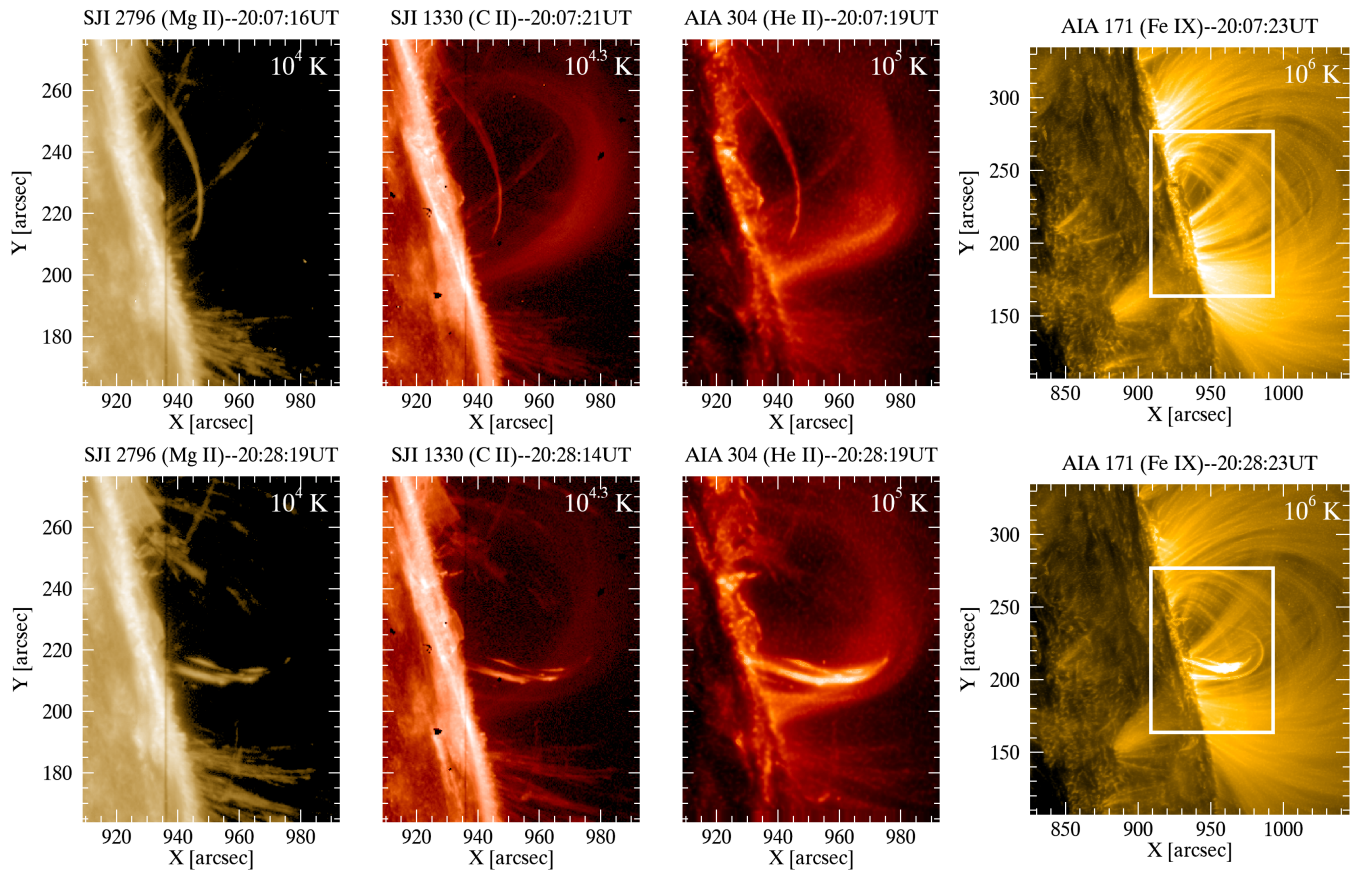


**Figure 1.** The studied active region (AR NOAA 12158) at the West limb of the Sun, observed by IRIS/SJI 2796 Å(left), SJI 1330 Å(second from left), and SDO/AIA 304 Å (third from left) taken at 20:07:16 UT (top) and 20:28:19 UT (bottom) on 2014 September 17 for the C-type flare. The separated panel on the right shows a wider FOV with SDO/AIA 171 Åover the same region, with the white rectangle outlining the FOV shown on the left panels. The top panels show a snapshot during the CE, while the bottom panels show a snapshot during the flare-driven rain. A movie of these rows is available. The movie shows off-limb coronal rain seen in the SJI 2796 Å, SJI 1330 Å, and AIA 304 Å falling towards the solar surface along coronal loop structures and chromospheric evaporation seen in the SJI 1330 Å and AIA 304 Å .

The mass and energy cycle of a flare loop is, therefore, bounded by two processes: chromospheric evaporation at the start and coronal rain at the end. From this perspective, it is interesting to compare the morphology, dynamics and

energetics of these two processes since, in the flare model, mass conservation already suggests a direct link between both. A first step in this direction has been taken by Jing et al. (2016), in which the sizes of the ribbons in Hα were observed to match the widths of the rain, thus suggesting a fundamental scale of the energy transport. Direct observations of chromospheric evaporation are, however, scarce. This is because of the large expected upward velocities of the heated material and the lack of resolution at very high temperatures. Previous studies and observations (most of them spectroscopic) showed that the speed of chromospheric evaporation in EUV and SXR wavelengths ranges from 50 to 800 km s$^{-1}$ (Doschek et al. 1994; Milligan & Dennis 2009; Young et al. 2015; Tian & Chen 2018; Li et al. 2022).

Coronal rain is another captivating phenomenon that is observed in the solar atmosphere. It is cool and dense partially ionised plasma that forms in a few minutes and falls toward the solar surface along loop-like trajectories (Antolin & Rouppe van der Voort 2012). Under quiescent conditions, its temperature and density varies between $10^3$–$10^5$ K and $\approx 10^{10}$–$10^{12}$ cm$^{-3}$, respectively. Coronal rain is best-observed off-limb, where it stands out clearly against the dark background. It can be seen in emission in both chromospheric (such as Hα, Ca II K & H and He I; De Groof et al. 2004; Schad 2018; Froment et al. 2020) and transition region lines (such as Si IV 1402 Å, or/and in He II 304 Å; Vashalomidze et al. 2015; Antolin et al. 2015). It is also observed generally in absorption on disk, where it often corresponds to supersonic downflows into sunspot umbrae (Kleint et al. 2014; Ahn et al. 2014; Chitta et al. 2016; Nelson et al. 2020; Chen et al. 2022). However, it is also accompanied by corona and upper transition region emission due to the Condensation Corona Transition Region (CCTR) (Antolin 2020). In quiescent active region conditions, thermal instability (TI) within a coronal loop in a state of thermal non-equilibrium (TNE), known as the TNE-TI scenario (Antolin 2020; Antolin & Froment 2022) is the leading cause of coronal rain generation. During TNE-TI, coronal heating concentrated towards the loop footpoints leads to chromospheric evaporation and, therefore, a density increase of the loop. If the heating is frequent enough, this increased density results in excessive radiative losses in the loop, surpassing the energy input from the heating mechanism, particularly around the loop apex (Müller et al. 2003, 2004). Consequently, TI arises, producing coronal rain. The exact role of TI remains a subject of ongoing debate (Klimchuk 2019). However, conditions leading to the onset of TNE are typically obtained in coronal loops characterized by strong stratification and high-frequency heating (Antiochos et al. 1999; Klimchuk & Luna 2019). The loop is subsequently drained, and the heating (evaporation) and cooling (condensation) restart, marking a TNE-TI cycle.

Coronal rain is typically observed in three different forms in the solar atmosphere (Antolin & Froment 2022). The most frequently observed form is called quiescent coronal rain, which occurs in coronal loops in active regions. The second form, flare-driven coronal rain, usually during the gradual phase of a solar flare (Foukal 1978; Scullion et al. 2016), is one of the most mesmerizing yet least understood phenomena observed in the solar atmosphere. The last form is called hybrid prominence/coronal rain complexes, which are formed in magnetic dips over null point topologies (Liu et al. 2016; Li et al. 2018; Mason et al. 2019; Chen et al. 2022).

Coronal rain morphology (lengths and widths) varies greatly according to the temperature of formation of the observed wavelength (due to differences in line opacities) and the spatial resolution of the instrument. At the smallest scales, observations in Hα of quiescent coronal rain report widths of $\approx$200-300 km with the Solar Swedish Telescope (SST) (Antolin & Rouppe van der Voort 2012; Froment et al. 2020), $\approx$500 km from EUV absorption in the HRI$_{EUV}$ passband (forming at $\approx 10^{5.9}$) with Solar Orbiter (Antolin et al. 2023) and ranges between 400 km and 900 km in SJI 2796 and 1400 passbands of IRIS (Antolin et al. 2015; Şahin et al. 2023). For a given wavelength, there is minimal difference in rain widths across various regions, as shown in Şahin et al. (2023), which suggests a fundamental MHD mechanism. The widths may be determined by magnetic topology and heating length scales (Antolin et al. 2022) or may be a characteristic of the cooling (for instance, set by TI, e.g. van der Linden & Goossens (1991)). The lengths, on the other hand, can vary significantly, from a few Mm up to tens of Mm according to Şahin et al. (2023), and it is unclear if there is a connection to temperature (Antolin & Rouppe van der Voort 2012; Antolin et al. 2015). Regarding the coronal rain dynamics, the average velocities vary between 40-70 km s$^{-1}$, with a long tail of 200-220 km s$^{-1}$ (Schrijver 2001; Antolin & Rouppe van der Voort 2012; Kleint et al. 2014; Schad et al. 2016; Şahin et al. 2023). The velocity of coronal rain is characterized by being lower than free-fall and is typically attributed to the presence of gas pressure forces (Oliver et al. 2014). Other candidates (such as ponderomotive force from transverse MHD waves) have also been proposed to explain this lower than free-fall acceleration. However, the observed wave amplitudes are typically insufficient to explain the rain dynamics (Verwichte et al. 2017).

Coronal rain shows spatial and temporal coherence. Neighbouring rain clumps follow similar trajectories and occur closely in time, thus defining a rain shower (Antolin & Rouppe van der Voort 2012). These rain showers indicate the

direction of the magnetic field and have a transverse length scale of a few Mm, and lengths of $\approx$27 Mm on average (Şahin & Antolin 2022). Şahin & Antolin (2022) use rain showers to properly identify coronal loops (as coronal plasma volume with similar thermodynamic evolution) and quantify the TNE-TI volume over an active region. They have estimated that at least 50% of the AR is subject to TNE. TI is thought to be responsible for the synchronisation of rain clumps within a rain shower (Fang et al. 2013, 2015a). In the TNE-TI scenario, the rain needs strongly stratified heating ($Q_{apex}/Q_{footpoint}$<0.1), sufficiently long-lasting and frequent enough ($\Delta_{heating} < \tau_{rad}$) and not too asymmetric across both footpoints (asymmetry in heating lower than 3) for TNE-TI (and thus coronal rain) to take place (Klimchuk & Luna 2019). This also seems incompatible with the flaring scenario since very strong but short heating is expected at the footpoints of flaring loops. The problem of the flare-driven coronal rain origin is further investigated by Reep et al. (2020) based on a 1D simulation study, in which they show that with the electron beam alone in a 1D setup, it is not possible to form any condensation.

For quiescent coronal rain, the observed downward mass flux of material is consistent with the estimated mass of the loop that is initially present (Antolin et al. 2015; Kohutova et al. 2019). However, this does not hold for any coronal structure that exhibits coronal rain. For instance, prominence/coronal rain hybrids show a much larger downward mass flux as coronal rain, with continuous downflows lasting over an hour when only 10 min or so would lead to a full depletion of the loop (Chitta et al. 2016). This apparent mismatch has been explained by the fact that these structures have magnetic dips at the top that act as large mass reservoirs (Chen et al. 2022). Here, we address this question for the flare context and investigate the flare-driven mass flux relative to that observed from chromospheric evaporation.

To investigate the role of flare-driven rain in the mass and energy circulation during a flare, it is important to investigate the similarities and differences between quiescent and flare-driven rain. Studies indicate that flare-driven rain can exhibit much large densities of $10^{13}$ $cm^{-3}$ in the clump core emitting in H$\alpha$ (Heinzel & Shibata 2018), an order of magnitude larger than the upper limit for quiescent rain. Jing et al. (2016), in H$\alpha$ with the Goode Solar Telescope (GST), have shown rain widths down to $\approx$120 km, half the width of the quiescent kind, which may be due to the increase in spatial resolution relative to the SST.

There have been no studies to our knowledge that directly compare the morphologies, dynamics and energetics between quiescent and flare-driven coronal rain. In this paper, we present the first high-resolution statistical study comparing these two types of coronal rain over a flaring AR. Furthermore, we also study the chromospheric evaporation observed by IRIS and AIA instruments and compare its mass and energy flux to that obtained from the rain. We present the data and method in Section 2 and Section 3, respectively. Then, we show detailed observational results in Section 4. Finally, in Section 5, we summarise and discuss the studied events.

## 2. OBSERVATIONS

We studied the active region (AR) of NOAA 12158, located at the west limb, which is shown in Figure 1. The data were taken by the Interface Region Imaging Spectrograph (IRIS; De Pontieu et al. 2014) and the Atmospheric Imaging Assembly (AIA; Lemen et al. 2012) on board the Solar Dynamics Observatory (SDO; Pesnell et al. 2012) on 2014 September 17 between 18:18:34 and 22:02:51 UT. During this period, a C2.1-class solar flare occurred in 19:29:11-20:24:26 UT time range.

**Table 1.** Observational time range with total average detected rain pixel per image for the SJI 2796, SJI 1330, and Cool AIA 304 for the pre-flare and gradual phases.

| Instruments | pre-flare phase | $N_{pixel}/N_{image}$ | gradual phase | $N_{pixel}/N_{image}$ | $\Delta$N |
|---|---|---|---|---|---|
| SJI 2796 | 18:18:40-19:29:06 | 585 | 20:24:42-22:02:56 | 1809 | 1224 |
| SJI 1330 | 18:18:34-19:29:01 | 216 | 20:24:37-22:02:51 | 1326 | 1110 |
| AIA 304 | 18:18:31-19:28:55 | 449 | 20:24:43-22:02:55 | 1746 | 1297 |

We use IRIS level 2 slit-jaw imager (SJI) 2796 and 1330 data, which are retrieved from the instrument website[1]. The SJI 1330 passband is dominated by the C II 1335.5 Å in the upper chromosphere/lower transition region forming at $10^{4.3}$ K, but emission from the Fe XXI 1354.08 Å coronal line forming at $10^{7.0}$ K can also be observed during flares. The emission from both can be easily differentiated based on its morphology: the hot emission is diffuse while the cool emission (e.g. from rain) appears clumpy. The SJI 2796 passband is dominated by 2796 Å emission from Mg II 2796.35 Å chromospheric line forming at $10^4$ K. The IRIS SJI obtained 10.36 s cadence images in the 1330 Å and 2796 Å over an area of $120''\times119''$ centred at [$936''$,$221''$] with an image scale of $0''.3327$ pixel$^{-1}$. In this study, we also used the IRIS spectrograph (SG) instrument, which has a cadence of 5.18 s (half of the SJI cadence) and an exposure time of 4 s, with a slit pixel size of $0''.33$ and length of $120''$ in sit-and-stare mode. For the SG data we focused on the Fe XXI 1354.08 Å line, the Mg II k 2796.02 Å line, and the Si IV 1402.77 Å line, with a formation temperature for the latter of $10^{4.8}$ K.

The SDO/AIA data also analyzed in this study are level 2 downloaded through the same instrument website as IRIS with a 12 s cadence. The AIA observations contain seven broad passbands (94 Å, 131 Å, 171 Å, 193 Å, 211 Å, 304 Å, and 335 Å). However, we focused on the AIA 304 Å channel dominated by He II 303.8 Å line (forming at $\approx 10^5$ K) for the rain detection and its analysis. The pixel size of AIA is $0''.6$ pixel$^{-1}$; however, for the purpose of co-alignment, we have rebinned the AIA data to match the SJI plate scale.

Based on the C2.1-class solar flare, we have divided our analysis into three parts: the pre-flare, impulsive and gradual phases. In the result section, we first present the analysis of the pre-flare and gradual phases and we focus on the impulsive phase. We provide the observational time range for the pre-flare and gradual phases in Table 1 for each instrument.

## 3. METHODOLOGY

### 3.1. *Data preparation*

We first resample the AIA images to match the IRIS SJIs and co-align them by matching the solar limb and using several characteristic features (such as bright points and filament patterns) on the disc and off-limb. We computed spatial shifts ($x$ and $y$) at various time instances using the images of AIA 304 Å and SJI 1330 Å. These shifts were then applied to all other AIA channels to align images with respect to the SJI images.

The AIA 304 Å channel exhibits a temperature response peak at $\approx 10^5$ K, resulting from He II 304 Å emission. However, the bandpass also includes an additional secondary peak at $\approx 10^{6.2}$ K, which can be attributed to many other spectral lines but in particular to Si XI 303.32 Å. When observing coronal rain off-limb, both components can have similar intensity. This similarity is due to the surrounding diffuse hot corona, being more extended along the line-of-sight (LOS) than the He II emission, which comes from the smaller, clumpy coronal rain (Antolin et al. 2015; Froment et al. 2020). To remove the hot emission from the AIA 304 passband, we follow the procedure by Antolin et al. (manuscript in preparation). We first fit the response function of AIA 304 over the hot temperature range with the other EUV passbands of AIA (which offer good coverage over the temperature range of $10^{5.5}-10^{7.2}$ K), as shown in Equation 1. Here, we take the response function using the *"aia_get_response"* command in *Interactive Data Language (IDL)* with the *chiantifix* and *eve* keywords, and specifying the time of the observation with the help of the CHIANTI (version 10) atomic database (Landi et al. 2012; Del Zanna et al. 2021). For further details, see Antolin et al. (2024).

$$R_{304,hot} = c_1 R_{94} + c_2 R_{131} + c_3 R_{171} + c_4 R_{193} + c_5 R_{211} + c_6 R_{335}$$
$$R_{304,cool} = R_{304,original} - R_{304,hot}$$

$$(1)$$

Here, $c_1...c_6$ are the coefficients obtained from least squares minimisation, for which the coefficients are c1=0.02982845, c2=0.02947056, c3=0.00012495, c4=0.00165538, c5=0.00952938, c6=-0.01288442. We will refer to those output images as Cool AIA 304 Å.

Figure 2 shows the resulting maps obtained using the Equation 1. The convolution of the new response function with the EUV passbands, therefore, provides the hot AIA 304 emission (right panel). The cool AIA 304 (middle panel) emission is then obtained by subtracting this hot component from the original AIA 304 (left panel) intensity. Further details on this procedure can be found in Antolin et al. (manuscript in preparation).
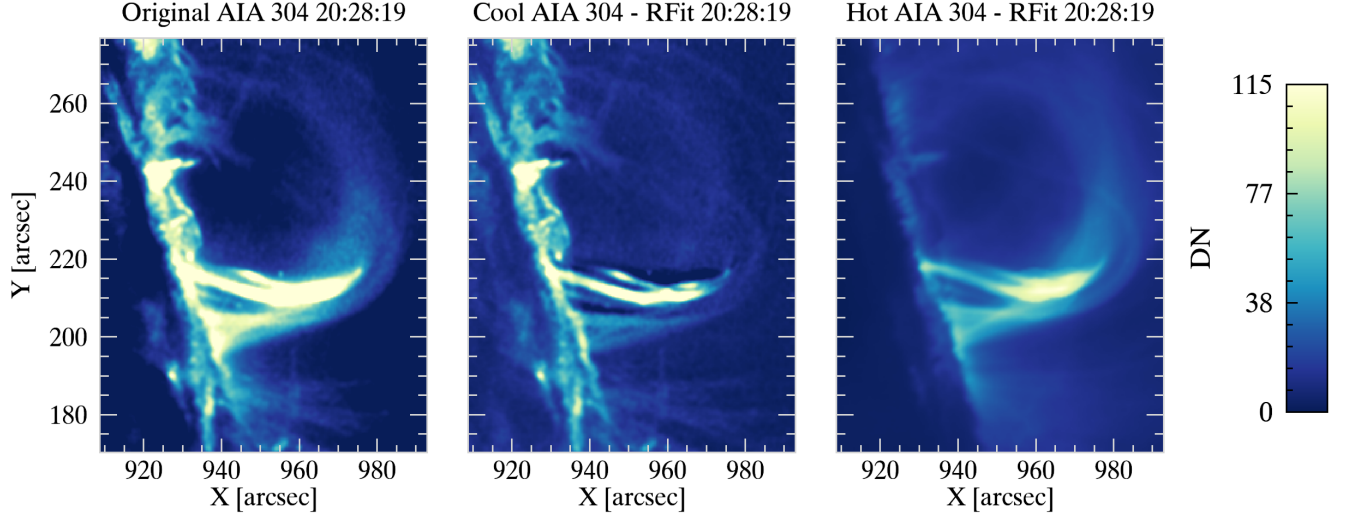
---

**Figure 2.** Comparison between original AIA 304 Å (left), cool AIA 304 Å (middle), and hot AIA 304 Å (right).

Similarly to the AIA 304 Å channel, the AIA 94 Å channel is blended with three temperature emissions from Fe XV, Fe XIV, and Fe XVIII. Here, in this study, we separated the hot Fe XVIII 93.96 Å line emission with a peak at $\approx 10^{6.85}$ K from the warm component in the AIA 94 Å channel since it is particularly important to study heating events (Testa & Reale 2012; Ugarte-Urra & Warren 2014). For this, we use the empirical method by Del Zanna (2013) to compute the hot contribution from a weighted combination of emissions from the AIA 94 Å, AIA 211 Å and AIA 171 Å channels (see Equation 2).

$$I_{FeXVIII} = I_{94} - \frac{I_{211}}{120} - \frac{I_{171}}{450} \qquad (2)$$

From now on, we will refer to those images as Fe XVIII, as opposed to the original AIA 94 Å.

### 3.2. *Coronal rain detection with imaging instruments*

Before using the semi-automatic coronal rain detection routine, we exclude the region surrounding the solar limb to avoid the significant brightness contrast. We exclude the spicular region above the limb by setting a minimum height of 6 Mm for off-limb observations. This eliminates most of the spicules and other cool chromospheric features that are typically seen above the solar surface. After that, to quantify the coronal rain material, we apply an automatic detection routine called the Rolling Hough Transform (RHT; Schad 2017) based on the Hough Transform (Hough 1962) developed by Schad (2017) and further tested for coronal rain detection by Şahin et al. (2023). First, the images are processed with a high-pass filter and converted to a binary scale before finally being processed with the RHT routine. Some parameters of the routine should be determined before execution for each channel (SJI 2796 Å  SJI 1330 Å and AIA 304 Å). The first parameter is the running mean filter and is determined according to the observed speeds in coronal rain. In this study, we used an 18-step ($\approx$ 3.1 min) for the SJI 2796 Å, SJI 1330 Å, and a 16-step running mean filter ($\approx$ 3.2 min) for the AIA 304 Å. We also use an 18-step bidirectional difference filter along the temporal axis for flow segmentation. Then, we chose the circular RHT kernel width ($D_w$) as 31 pixels for all channels according to the observed minimum length of the rain. This kernel width ($D_w$) is centred on each image pixel to be evaluated at one time. The last parameter that must be specified is the standard deviation regarding the background noise $\sigma_{noise}$. We use 1.1 DN for the SJI 2796 Å, SJI 1330 Å and 1.4 DN for the AIA 304 Å. The influence of these parameters and further discussion can be found in Şahin et al. (2023). Using these parameters, the RHT algorithm produces spatial and temporal information on the mean axial direction, the resultant length, the error in the mean axial direction and the peak of the RHT function. All these outputs have three dimensions in terms of positions (x and y) and time (t). Please refer to Schad (2017) and Şahin et al. (2023) for details on these parameters. In this study, we only include the pixels for which $\overline{R}_{xy} \geq 0.85$, $max[H_{xy}(\theta)] \geq 0.8$, $\overline{R}_t \geq 0.85$, $max[H_t(\theta)] \geq 0.8$ for all channels, and $\overline{|\theta_t|} \leq 85°$ for the AIA 304 Å and $\overline{|\theta_t|} \leq 84°$ for both SJI channels, since these values ensure relatively small errors for projected velocities.
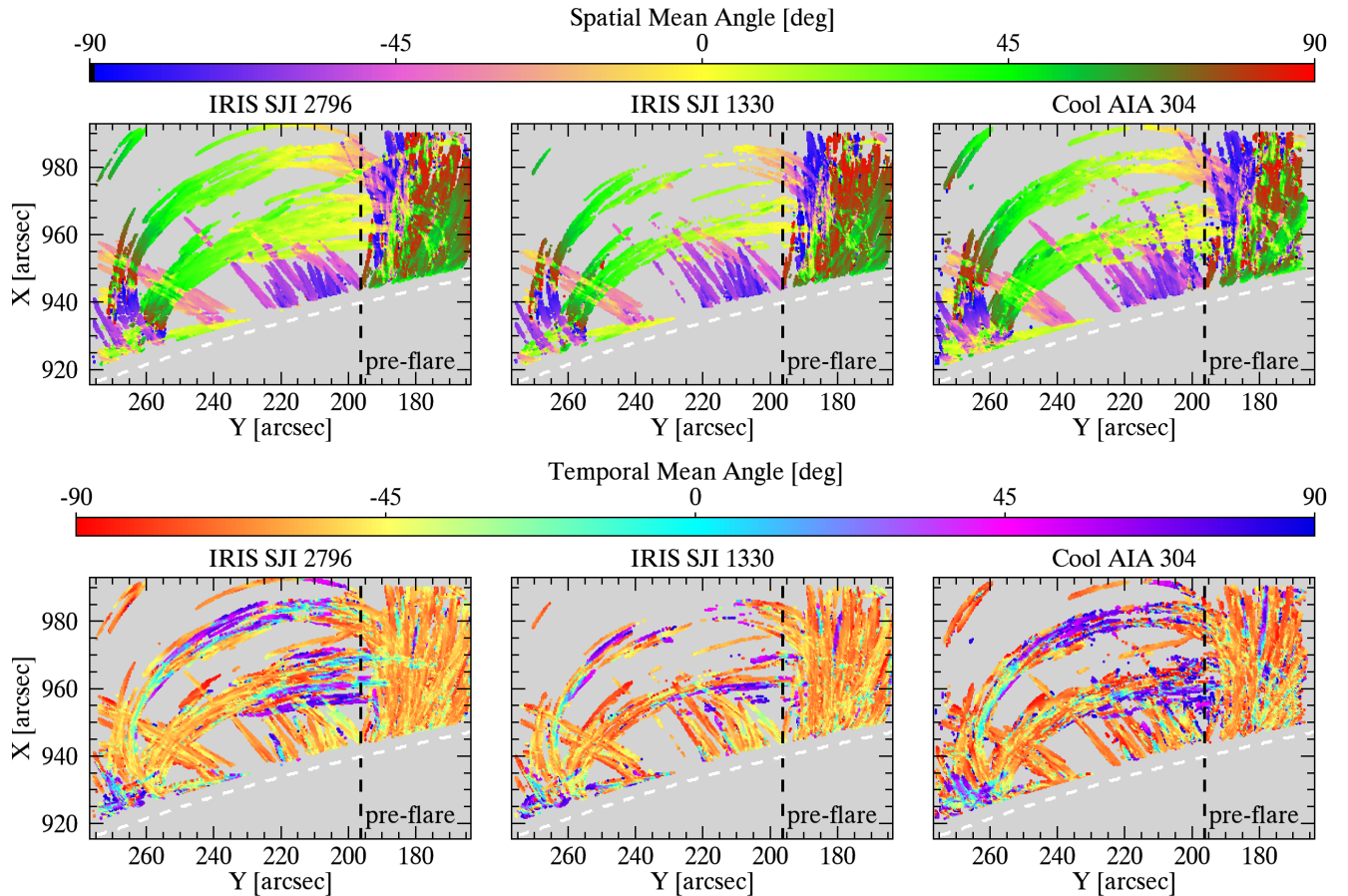
**Figure 3.** Average spatial mean angle (top) and temporal mean angle (bottom) maps over the entire time sequence of the pre-flare phase as derived using the Rolling Hough Transform routine. Average temporal mean angle maps show both downward (negative values) and upward (positive values) motions. The spatial mean angle maps indicate the inclination of the rain with respect to the horizontal direction, while temporal mean angle maps indicate the dynamical change along a trajectory. The dashed white lines indicate the solar limb. The right side of the vertical black dashed line represents the quiescent coronal rain that is observed at all times.

### 3.3. *Chromospheric evaporation and coronal rain detection with IRIS/SG*

For this sit-and-stare observation the IRIS slit is located at the footpoint of the flaring loop, which allows to see the dynamics and temperature of the CE episodes we investigate. However, due to the West limb location and the later times of the rain showers compared to CE, we could only capture one of the analysed the rain shower episodes.

For the CE we select the Fe XXI 1354.08 Å and Si IV 1402.77 Å lines. For the rain shower, we consider the Si IV and Mg II k lines but focus on the former since Mg II k can be optically thick at the low TR heights where the slit is located. For each time step, we select all points along the slit whose spectra are above 5 DN and 8 DN, respectively for the Fe XXI and Si IV lines. The number of consecutive points in the wavelength dimension above this threshold needs to be larger than 5. Due to the low count rate of the Fe XXI line, we only fit a single Gaussian for this line, but we allow either a single or a double Gaussian for the Si IV line. We select the best fit taking the lowest $\sigma$ error from the fit and also setting a maximum error threshold for each line. We further avoid extremely thin profiles by setting a lower threshold based on the peak temperature formation of the line (we choose 0.13 Å and 0.018 Å for the Fe XXI and Si IV lines, respectively). We also allow for the occurrence of additional spectral components in complex profiles. For this, we subtract the result of the fitting (single or double Gaussian) to the original profile and fit the resulting profile subject to the same conditions as for the original profile. In total, a complex line profile is allowed to have 4 distinct spectral components (for example, a main profile fitted with a single or double Gaussian, and 2 residuals to the left and right of the spectrum).

We calculate the spectral quantities from the Gaussian fitting in the usual way, with the position of the peak of the fitting equal to the Doppler velocity, and the FWHM of the line ($\sigma 2\sqrt{2\log 2}$, with $\sigma$ the Gaussian width) equal to the line width. The errors from the fit provide the corresponding errors in the measurement. The nonthermal velocity $v_{nth}$ is calculated as follows:

$$v_{nth} = \sqrt{\left(\frac{\sigma c}{\lambda_0}\right)^2 - \frac{k_B T}{m_A} - \left(\frac{W_{inst} c}{\lambda_0 2\sqrt{\log 2}}\right)^2}, \tag{3}$$

where $\lambda_0$ is the rest wavelength of the line, $k_B$ is the Boltzmann constant, $c$ is the speed of ight, $m_A$ is the atomic mass of the element and $W_{inst}$ is the instrumental broadening (equal to the IRIS FUV broadening of 26 Å).

## 4. RESULTS

### 4.1. *Quiescent and Flare-driven Coronal Rain*

#### 4.1.1. *Spatial and Temporal Perspective*

We first examine the pre-flare and gradual phases, where we observe the quiescent and flare-driven coronal rain, respectively. For this purpose, we utilize data from the SJI 2796 Å, SJI 1330 Å, and AIA 304 Å channels. Figure 3 presents the average spatial (top panels) and temporal (bottom panels) mean angle maps obtained from the RHT algorithm during the pre-flare phase, while Figure 4 shows the same information but for the gradual phase. The spatial mean angle is associated with the inclination of the coronal rain observed in the plane-of-the-sky (POS), whereas the temporal mean angle indicates the dynamic variations occurring along the trajectory of the coronal rain. The coloured pixels on these maps represent coronal rain, and the negative values in the temporal mean angle maps (bottom panels in Figure 3 and Figure 4) indicate the downward motion of coronal rain. As can be seen in these maps, downward motions are dominant due to gravity's force. In these figures, the dashed white lines indicate the solar limb. We also divide these maps into two regions with dashed black lines. The rain in the region to the right is observed during the entire observation time (i.e. from pre-flare to the gradual phases, including the impulsive phase), with apparently little variation, indicating that it is not part of the flare loop. We refer to it as neighbouring coronal rain, and it is not included in our analysis (subject of future work).

Table 1 provides information about the observational time for the pre-flare and gradual phases and the number of average and maximum detected rain pixels per image in the right column of each phase time. It is worth noting that in the pre-flare phase, we have considered the average number of detected rain pixels, while in the gradual phase, we took the maximum detected rain pixels per image. This can be justified given the relatively constant and increasing rain quantity in the pre-flare and gradual phases, respectively. The detected average rain pixel per image is 585, 216, and 449 for the pre-flare phase in the SJI 2796 Å, SJI 1330 Å and Cool AIA 304 Å, respectively, while the maximum detected rain pixel per image is 1809, 1326, and 1746 for the gradual phase. We would like to highlight that these average numbers are based on the left side of the vertical dashed black line shown in Figure 3 and Figure 4. Even though some horizontal loops (on the left side) have footpoints on the right-hand side of the vertical dashed line, we capture most of these loops (and the respective rain) on the left-hand side. As shown on the bottom-left plot in Figure 5, the quantity of rain in SJI 2796 Å, SJI 1330 Å, and Cool AIA 304 Å seems to change by roughly the same amount from pre-flare to the gradual phase. However, this is not reflected by the percentage because the initial amounts are different. In order to measure the amount of flare-driven rain, we subtract the average values found in the pre-flare phase, and the results of this subtraction ($\Delta$N) are provided in the last column. It can be seen that these values are very similar to each other in terms of numbers, with similar trends. Remarkably, the SJI 1330 Å displays the lowest values in contrast to SJI 2796 Å and Cool AIA 304 Å, possibly due to lower opacity in SJI 1330 Å (Leenaarts et al. 2013; Rathore & Carlsson 2015), and thereby making the rain more difficult to detect.

We also examine the relationship between the detected rain pixel number and coronal rain intensity over the solar limb (roughly 8 Mm to avoid eruption occurring in the limb). The top panels in Figure 5 show the detected rain pixels at one particular time (20:36 UT) for the SJI 2796 Å, SJI 1330 Å, and Cool AIA 304 Å. In these panels, the coloured pixels correspond to the spatial mean angle. In the bottom panels, we provide information on the quantity of these detected rain pixels (left) and the average intensity variation (right) above the limb over the observation time. The increase in intensity shows a similar trend as the increase in quantity. The average intensity above the limb exhibits a corresponding increment by a factor of 3.14, 2.95, and 4.35 from pre-flare to the gradual phases for the SJI 2796 Å, SJI 1330 Å, and Cool AIA 304 Å, respectively. Cool AIA 304 Å has higher intensity than in the SJI 2796 Å and SJI 1330 Å. One potential explanation could be associated with opacity, where non-equilibrium ionisation effects
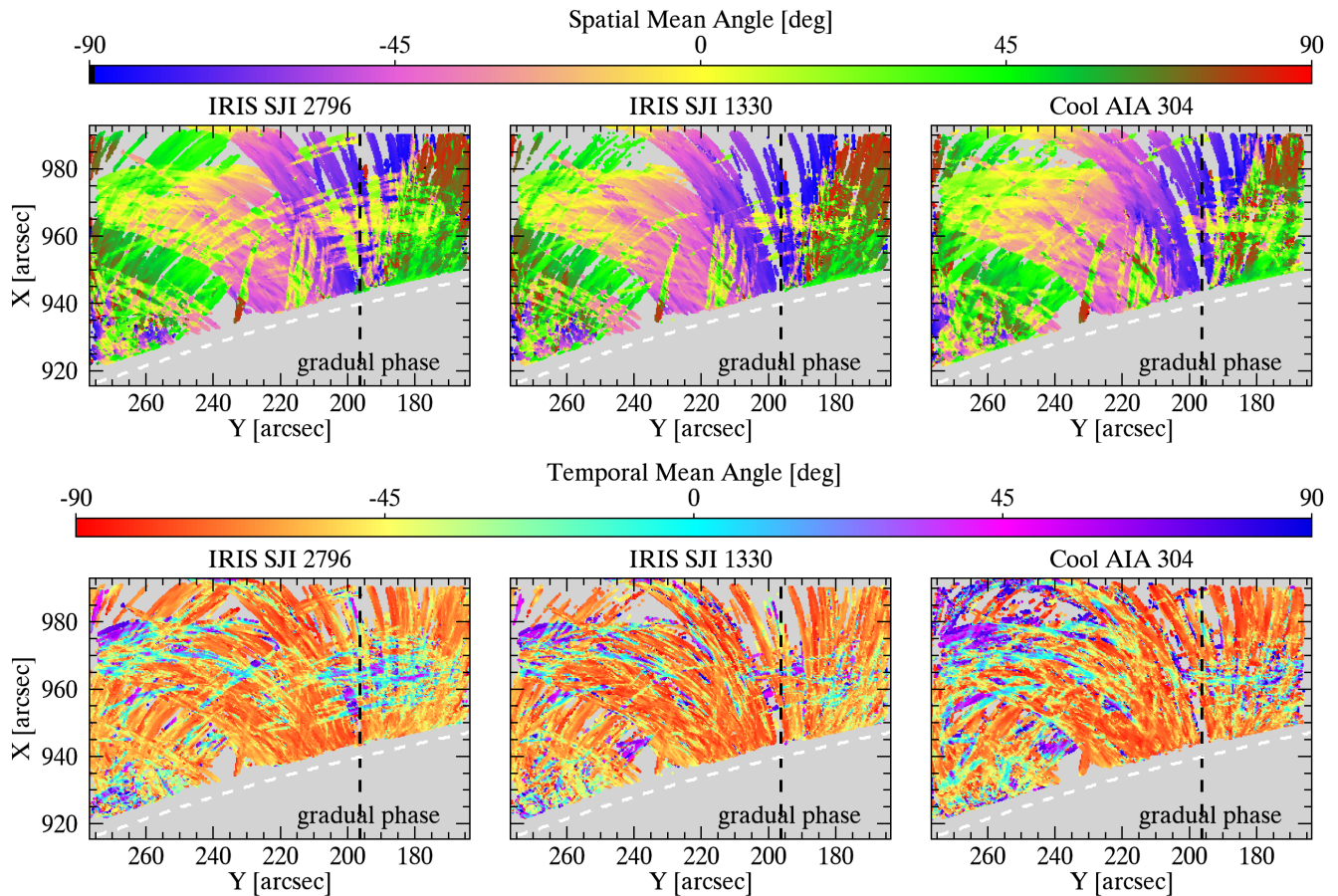
**Figure 4.** The same maps as shown in Figure 3 but for the gradual phase.

**Table 2.** Increase factor in intensity and quantity from pre-flare to gradual phases.

|  | SJI 2796 | SJI 1330 | AIA 304 |
|---|---|---|---|
| Intensity | 3.14 | 2.95 | 4.35 |
| Quantity | 3.09 | 6.15 | 3.89 |

greatly enhance the He II emission (Golding et al. 2017). Additionally, it is conceivable that the observed variations are influenced by the morphology of rain in these channels, with the rain appearing larger in the AIA 304 channel compared to the SJI channels, possibly attributed to differences in resolution (0.87 Mm for the AIA and 0.48 Mm for the SJI channels) (Şahin et al. 2023). Although coronal rain occupies a large POS area on the AR in both phases (see also Figures 3 and 4), it is clear that the rain quantity also increases. Quantifying this variation, we have an increase by a factor of 3.09, 6.15, and 3.89 from pre-flare to the gradual phases for the SJI 2796 Å, SJI 1330 Å, and Cool AIA 304 Å, respectively. Information on this increase in intensity and quantity is given in Table 2. On the bottom-right panel, the big increase in SJI 1330 Å (between two vertical dashed lines) corresponds to chromospheric evaporation (CE) and is not included in the calculation of rain quantity and intensity since it is not part of the gradual phase. The starting time for the gradual phase is given by the purple vertical dashed lines ($t_{Rain}$).

### 4.1.2. *Dynamics of Rain Clumps*
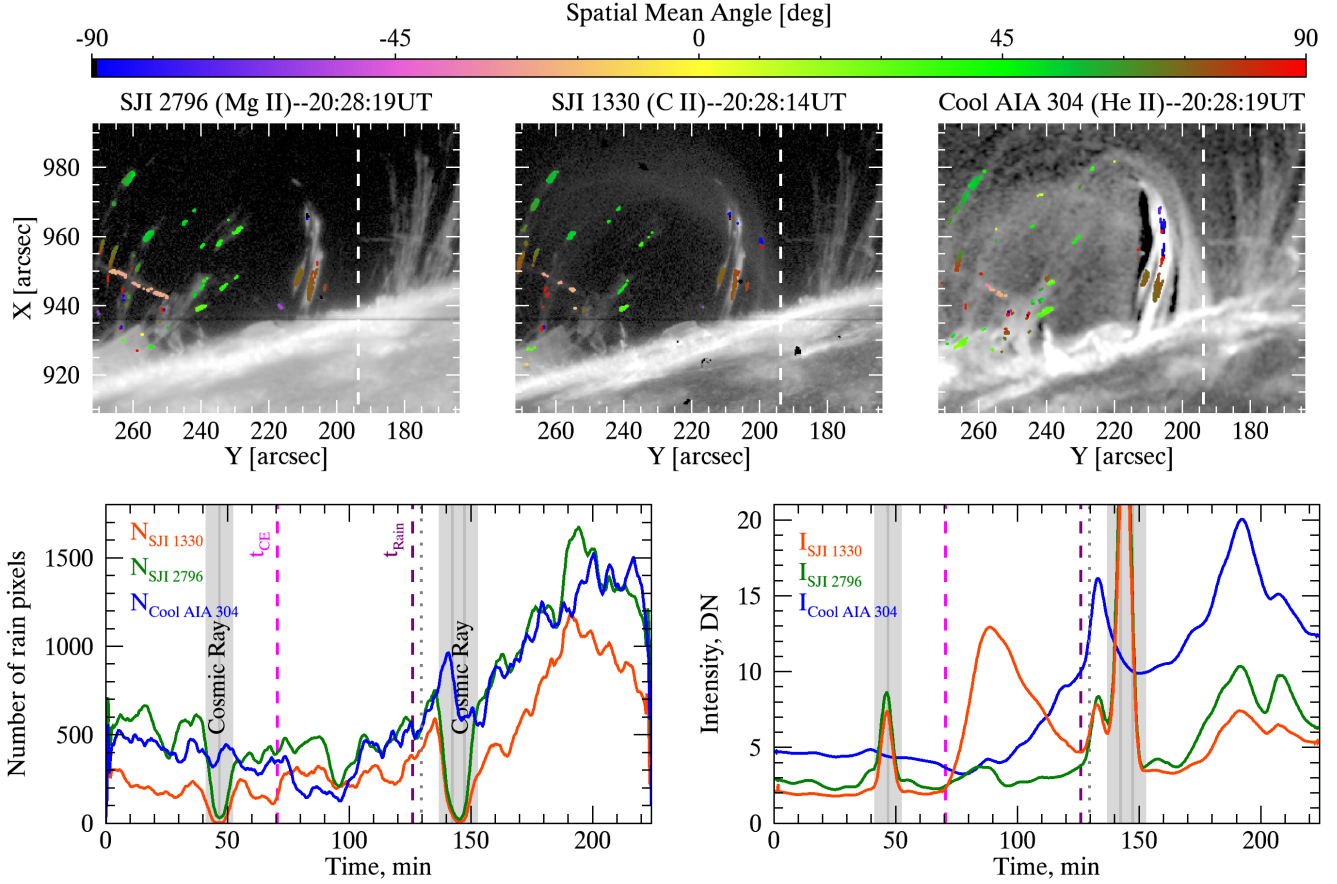
**Figure 5.** Top: Detected rain pixels at 20:28 UT in SJI 2796 Å (left), SJI 1330 Å (middle) and Cool AIA 304 Å (right). Coloured pixels correspond to the spatial mean angle. Bottom: rain pixel number (left) and rain intensity (right) variation over the entire observational time for the SJI 2796 Å (green), SJI 1330 Å (red), and cool AIA 304 Å (blue). Here, the grey-shaded areas depict where the cosmic ray happens in the SJI channels. The pink and purple dashed lines represent the start time of the CE and gradual phase (rain), respectively. The vertical dotted lines indicate the time of the top panels. An accompanying movie is also available and shows the detected rain pixels in terms of spatial mean angle during the observation time. Note that all curves are 20-point smoothed versions of the averaged number of rain pixels and intensity.

We are now shifting our focus to the analysis of rain clump dynamics. We first show the projected velocity of each rain clump over the pre-flare and gradual phases in Figure 6 and Figure 7, respectively. Using the Equation 4 (Schad 2017), we obtained the velocity for each curved path.

$$v_{||} = \tan \overline{\theta}_t (\frac{\delta x}{\delta t}). \tag{4}$$

Here, $\delta t$ and $\delta x$ represent the average cadence and spatial sampling on the given date, respectively. $\delta x$ is 242.51 km for the SJI channels and 242.44 for the AIA channel. $\delta t$, on the other hand, is 10.36 s and 12 s for the SJI and AIA channels, respectively. Then, the horizontal and vertical velocities are calculated using Equation 5 and Equation 6, respectively, through the RHT spatial mean angle $(\overline{\theta}_{xy})$.

$$v_x = v_{||} \cos \overline{\theta}_{xy} \tag{5}$$

$$v_y = v_{||} \sin \overline{\theta}_{xy} \tag{6}$$

Using Equation 5 and Equation 6, tangential (Equation 7) and radial (8) velocity components are derived:

$$v_{tan} = -\cos(\alpha)v_x + \sin(\alpha)V_y \tag{7}$$

**Table 3.** Increase factor in downflow and upflow projected velocity from pre-flare to gradual phases.

|          | SJI 2796 | SJI 1330 | AIA 304 |
|----------|----------|----------|---------|
| Downflow | 1.38     | 1.51     | 1.33    |
| Upflow   | 1.01     | 1.25     | 1.05    |

$$v_{rad} = \sin(\alpha)v_x + \cos(\alpha)V_y \tag{8}$$

where $\alpha$ represents the angle between the radial and horizontal directions in radians. These equations provide the projected velocity as shown in Equation 9.

$$v_p = |v_{||}| = \sqrt{v_{tan}^2 + v_{rad}^2} \tag{9}$$

We show the average projected velocity maps for downflow and upflow motions in Figure 6 and in Figure 7, corresponding to the pre-flare and gradual phases, respectively, across the SJI 2796 Å, SJI 1330 Å, and Cool AIA 304 Å channels. The majority of coronal rain clumps exhibit increased downward speeds at lower heights, suggesting an acceleration while falling. This is particularly evident during the gradual phase. We also present 1D histogram plots of projected velocity in Figure 8 for downflows (left) and upflows (right) for the pre-flare (top) and the gradual phases (bottom). Note that we obtained these plots focusing on the left side of the vertical dashed lines in Figures 6 and 7. It is apparent that both downflow and upflow speeds range from a few km s$^{-1}$ up to 220 km s$^{-1}$, and the overall shape of these velocity distributions is very similar across the channels for each phase. The median downflow velocities are found 34±28 km s$^{-1}$, 34±28 km s$^{-1}$, and 38±27 km s$^{-1}$ during the pre-flare phase and 47±35 km s$^{-1}$, 52±40 km s$^{-1}$, and 51±38 km s$^{-1}$ for the gradual phase in SJI 2796 Å (green), SJI 1330 Å (blue), and Cool AIA 304 Å (red), respectively. On the other hand, these median velocities are 37±41 km s$^{-1}$, 38±42 km s$^{-1}$, and 47±46 km s$^{-1}$ for the upflow projected velocity during the pre-flare phase and 38±44 km s$^{-1}$, 48±53 km s$^{-1}$, and 50±48 km s$^{-1}$ for the gradual phase in the SJI 2796 Å (green), SJI 1330 Å (blue), and AIA 304 Å (red), respectively. Cool AIA 304 Å has consistently higher speeds than the SJI channels in the pre-flare phase in both up and downflow motions. The downflow velocity results indicate a factor of 1.38, 1.51, and 1.33 increase in velocity from the pre-flare to the gradual phases for the SJI 2796 Å, SJI 1330 Å, and Cool AIA 304 Å, respectively. The upflow velocities show almost no change (factors of 1.01 and 1.05 increase for the SJI 2796 Å and Cool AIA 304 Å, respectively), or very little change (factor of 1.25 increase for SJI 1330 Å) from the pre-flare to the gradual phase (see Table 3). We suspect that this discrepancy is due to the very local and sporadic nature of the upflows (further explanation is given below), for which spatial resolution becomes more important, occurring at temperatures higher than the chromospheric range of SJI 2796 Å.

We also examined the behaviour of the average downflow and upflow motions over the projected height during the pre-flare and gradual phases. However, in Figure 9, we only show this for the gradual phase since we obtain similar trends during the pre-flare phase. Here, the solar limb is given by zero height. As the rain falls (from roughly 43 Mm to the solar limb), its average downflow projected velocities show a similar trend at all heights, except near the top of the loops (from 43 Mm to 35 Mm), where a clear increase in speeds (roughly from 42 km s$^{-1}$ to 70 km s$^{-1}$) is seen. This small acceleration followed by constant downward speed is expected from gas pressure (Oliver et al. 2014). However, it is also likely that projection effects play a role since stronger projection is expected near the loop apex (and therefore smaller speeds). Relative to the downward motion, the upflow projected velocities exhibit more stochastic behaviour. In order to show this behaviour better, we focus on one particular shower event (which we later named shower1 or SH1) in Figure 10. Here, downflow motions (positive values) are the bulk motions, whereas the upflow motions (negative values) are more localised and sporadic in time.

### 4.1.3. *Morphology of Rain Clumps*

We also present the statistical analysis of the width and length of individual rain clumps during the pre-flare and gradual phases. The width and length are calculated in the same way as we described in our previous paper by Şahin
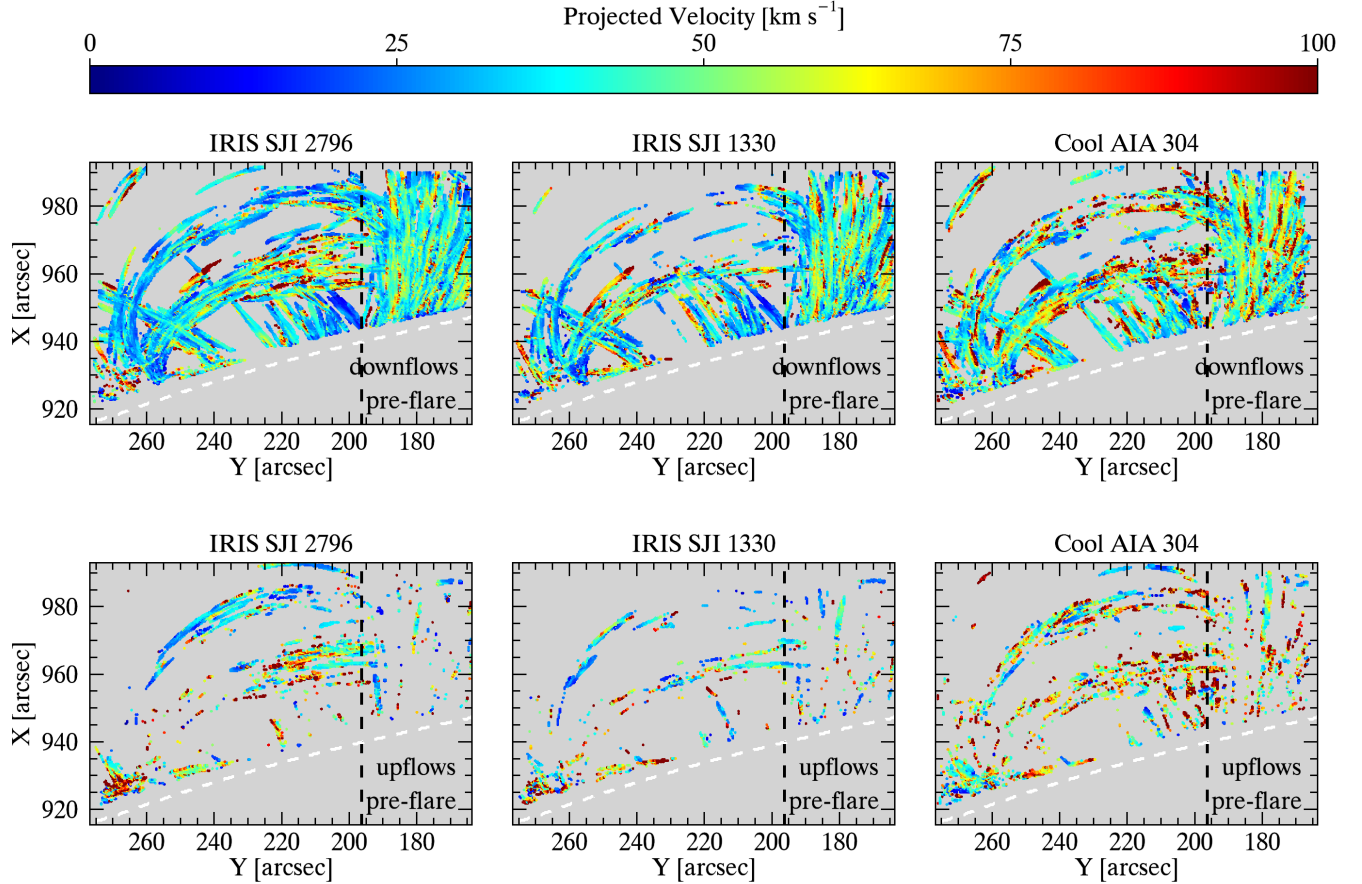
**Figure 6.** Average downflow (top panels) and upflow (bottom panels) projected velocities in SJI 2796 Å (left), SJI 1330 Å (middle), and AIA 304 Å (right) over the pre-flare phase. The dashed white lines over the plots indicate the solar limb. The right side of the vertical black dashed lines represents the quiescent coronal rain that is observed at all times.

et al. (2023). In a nutshell, the width of each rain clump is determined by fitting a Gaussian to the intensity profile along a perpendicular line to the clump's trajectory and calculating the Full Width at Half Maximum (FWHM). To compute the length of the clumps, the center point of the Gaussian fit used for the width calculation is determined, and a straight path is drawn along the same trajectory. The extrema of the clump's length is defined by points where the intensity falls below noise thresholds along the straight path, and the average length is calculated based on these measurements (see Figure 9 in Şahin et al. (2023)). In Figure 11, we show the 1D histogram distribution (top panels) of the rain clump widths in the SJI 2796 Å (green), SJI 1330 Å (blue), and Cool AIA 304 Å (red) during the pre-flare (left) and gradual phases (right). It is apparent that these distributions are similar in shape across all channels in each phase.

We found that the average widths are 0.79±0.22 Mm, 0.73±0.22 Mm, and 1.23±0.36 Mm for SJI 2796 Å, SJI 1330 Å, and Cool AIA 304 Å, respectively, in the pre-flare phase. These results are consistent with those shown in our previous paper (e.g., Şahin et al. 2023) where we only focus on the quiescent coronal rain. As discussed in that paper, it is likely that the higher opacity and lower spatial resolution of AIA 304 Å are mainly responsible for the larger widths in that channel. These widths increased by a factor of 1.10, 1.04, and 1.02 in the gradual phase and were found to be 0.87±0.27 Mm, 0.76±0.24 Mm, 1.25±0.37 Mm for the SJI 2796 Å, SJI 1330 Å, and AIA 304 Å, respectively. However, these increases fall within the range of standard deviation (although SJI 2796 Å appears to hold greater relevance), implying that they may lack statistical significance. The bottom plots in the same figure show the width variation with height, where $z = 0$ indicates the solar limb. In both pre-flare (left) and gradual (right) phases, the widths remain roughly stable as the rain falls. However, we can distinguish a positive trend in the pre-flare phase in the high-resolution SJI 2796 and 1330 images, with widths increasing 100-200 km on average as they fall from the higher ($\approx 32$ Mm) to the low ($\approx 5$ Mm) corona. This trend is not seen in the gradual phase, where widths are largely
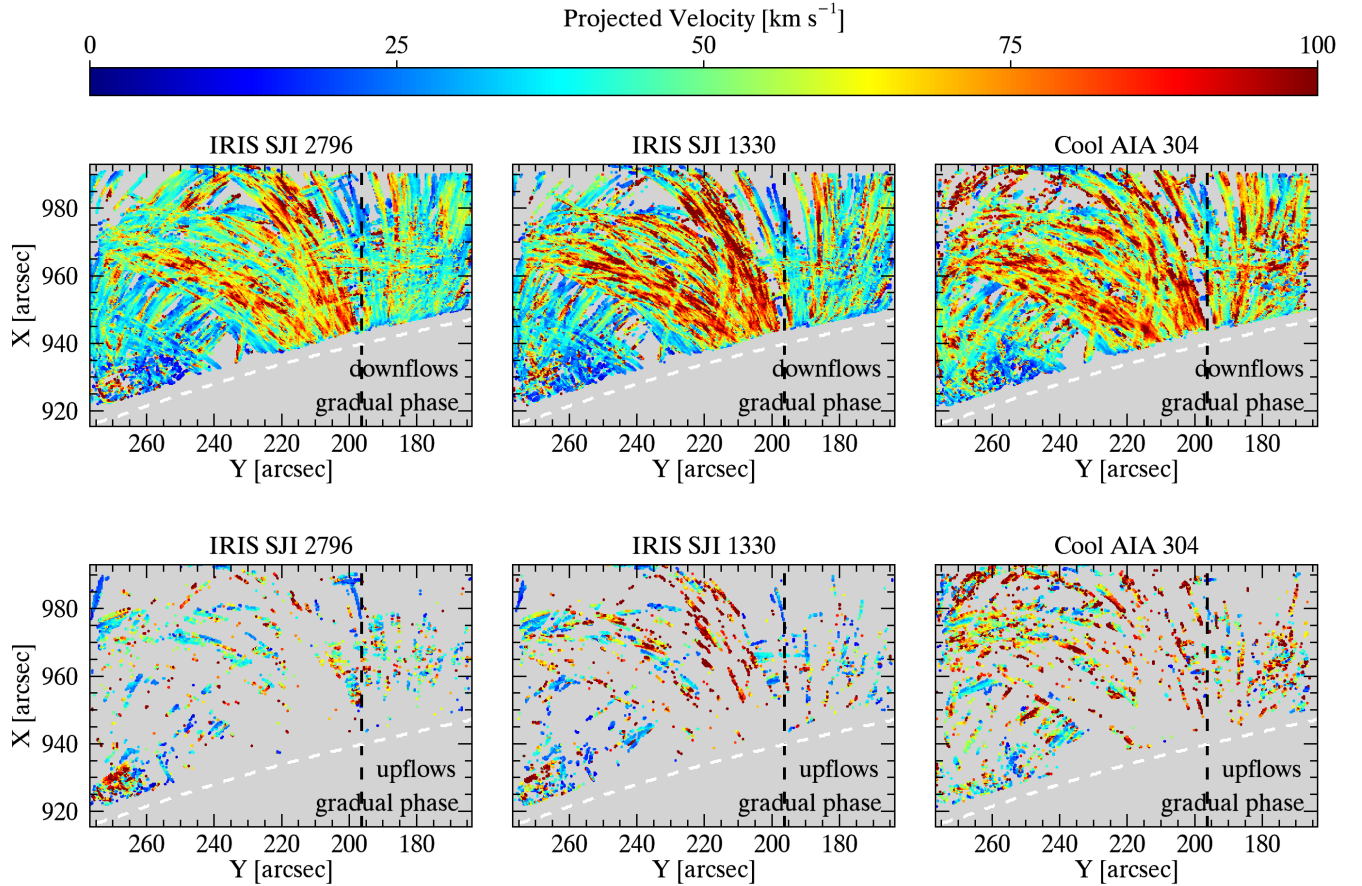
**Figure 7.** The same maps as shown in Figure 6 but for the gradual phase

constant with height. This pre-flare increment could be simply due to the fact that rain appears high up and, even if very rapid, takes some time to grow. In the gradual phase, rain is seen everywhere, particularly in the lower loop portions, reducing this effect. We further note that the widths in the SJI 2796 Å are consistently larger than those in the SJI 1330 Å by ≈100 km, for both pre-flare and gradual phase. This may also be due to the opacity difference. These effects are also observed in our previous study (e.g. Şahin et al. (2023)), where we analyzed SJI 2796 Å and SJI 1400 Å.

We also show the distribution of the rain clump length in Figure 12 during the pre-flare (left) and gradual (right) phases. We found that the average lengths are 5.12±3.50 Mm for the SJI 2796 Å, 4.50±3.16 Mm for the SJI 1330 Å, and 6.68±5.99 Mm for the Cool AIA 304 Å. These lengths increased by a factor of 1.50, 1.54, and 1.20 in the gradual phase and were found to be 7.66±5.46 Mm, 6.94±5.28 Mm, 7.99±7.17 Mm for the SJI 2796 Å, SJI 1330 Å, and Cool AIA 304 Å, respectively. As for the widths, we find a small increase in the lengths in the pre-flare phase of 1000-2000 km with decreasing height for all channels, from 30 Mm down to a height of 13 Mm or so. On the other hand, for the gradual phase, we do not see any trend in any channel, and the lengths become similar, which could simply be attributed to the large quantities of (multi-thermal) rain rapidly occupying the entire loop (clump lengths become roughly 20% of half of the loop length). Below 13 Mm, we see a strongly decreasing, linear trend of the lengths of all channels for both pre-flare and gradual phases, down to 4000-5000 km at a height of 3000 km. This strong decrease is also obtained for previous datasets (Şahin et al. 2023) and can be simply explained by the clumps crossing below the solar limb and the inability of the RHT to continue tracking them.

We find that the SJI 2796 Å lengths are significantly larger than in the SJI 1330 Å by 1000-2000 km in the pre-flare phase. In turn, the lengths are 2000-3000 km larger in the Cool AIA 304 Å than in the SJI 2796 Å(see Figure 12). This may be due to the higher opacity and lower resolution of the AIA 304 line. Strong intensity variation along a
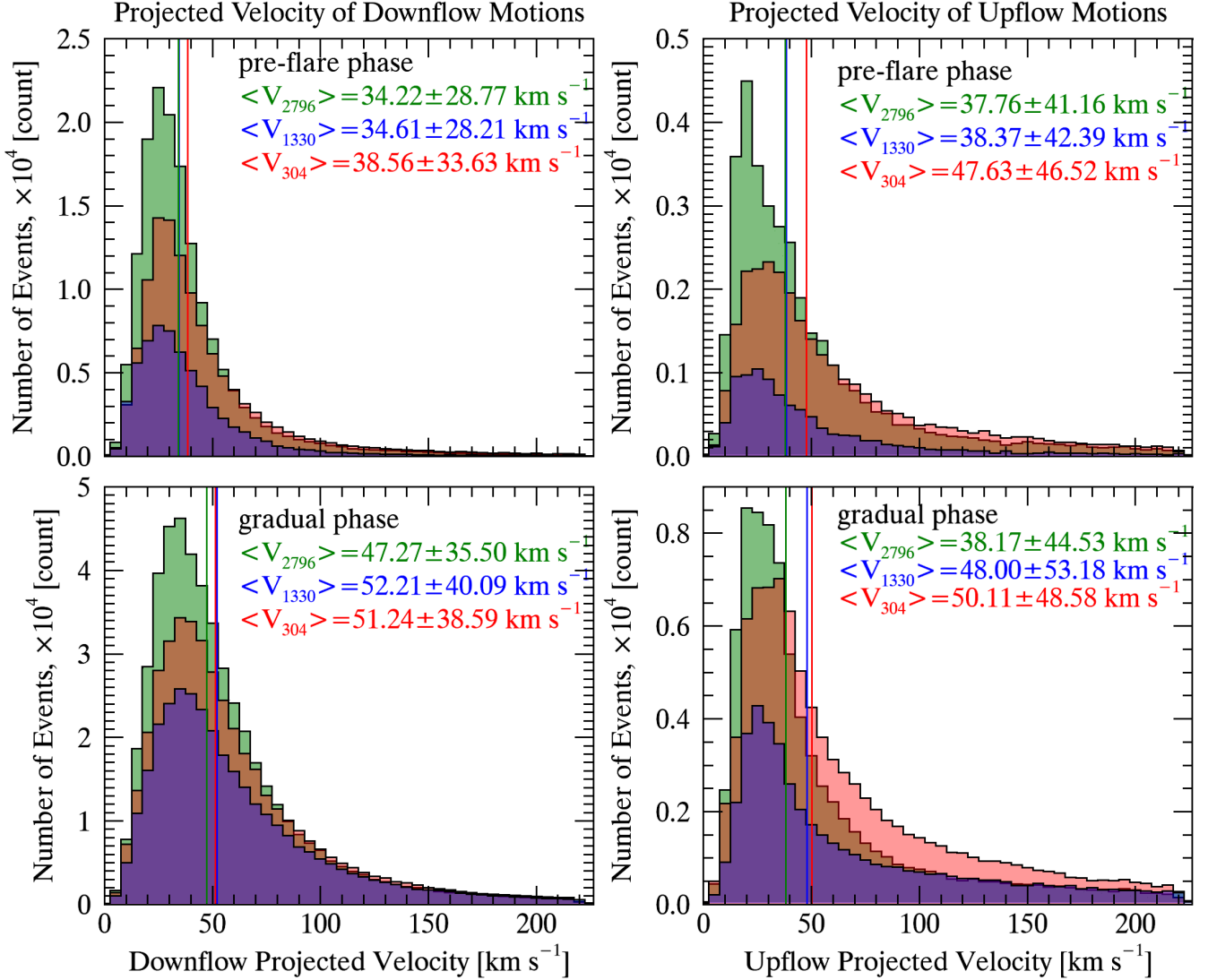
**Figure 8.** Top: 1D histogram distribution of the projected velocities during the pre-flare phase for the downflow (left) and upflow (right) motions in SJI 2796Å (green), SJI 1330Å (blue), and AIA 304Å (red), with the corresponding mean and standard deviation in the inner caption. Bottom: Same as the top panels, but for the gradual phase.

clump can be interpreted as separate clumps in our algorithm. However, lower resolution reduces these variations, leading to longer clumps with smoother intensities along their lengths.

### 4.2. *Chromospheric Evaporation*

Flare ribbons observed in chromospheric lines like Hα, directly signify the influence of electron beams on the chromosphere, and mark the initiation of chromospheric evaporation (CE). We start our analysis by investigating the impulsive phase of the solar flare, where we see the flare ribbons and CE (i.e. hot regions). CE occurs between 19:29 and 20:24 UT time range. The diffuse emission signature of CE can be clearly seen in the SJI 1330 Å and (hot) AIA 304 Å channels in Figure 1, as well as in the hotter AIA channels. The SJI 2796 Å and the Cool AIA 304 Å passbands show an absence of this evaporation.

#### 4.2.1. *Chromospheric Evaporation Dynamics*

We also applied the RHT algorithm to SJIs and Cool AIA data during the impulsive phase and then obtained the projected velocity maps (see Figure 13) for the downflow (top panels) and upflow (bottom panels) motions. As can be
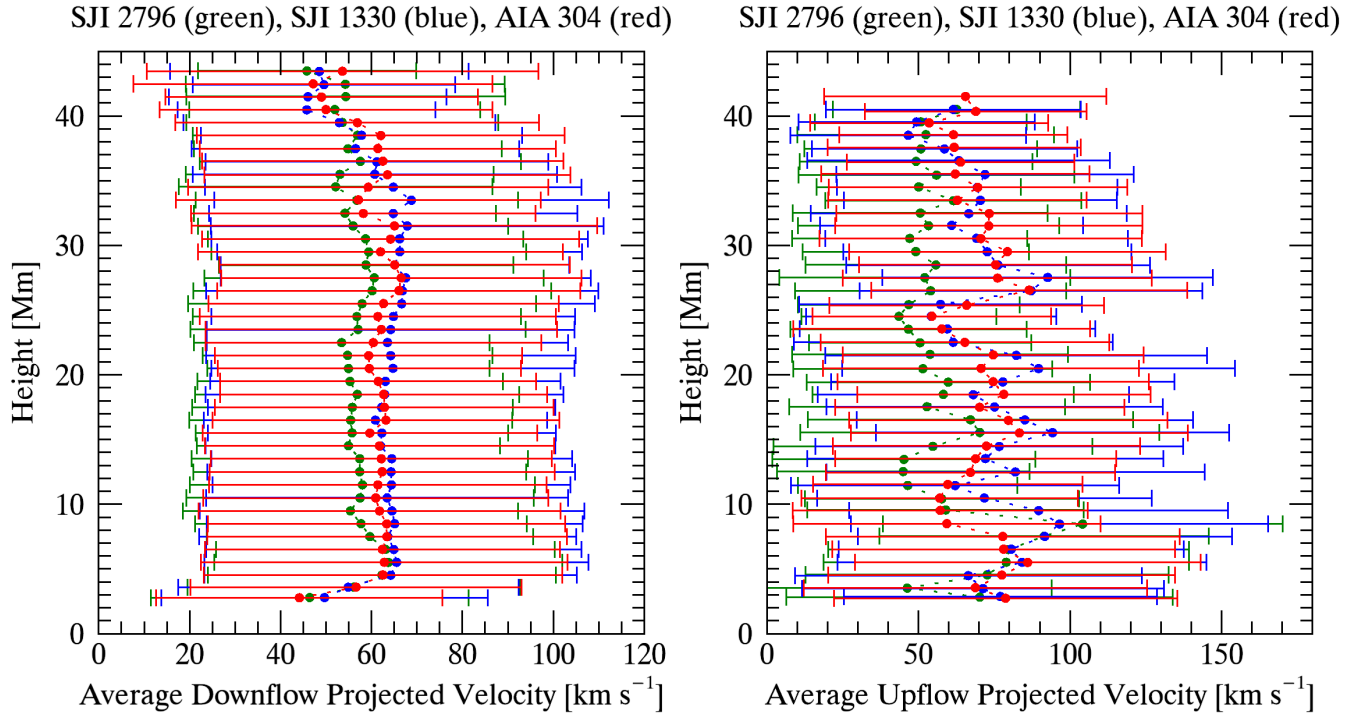
**Figure 9.** The variation of the downflow (left) and upflow (right) motions and their standard deviation at each height bin during the gradual phases. Green, blue and red colors denote SJI 2796 Å, SJI 1400 Å, and AIA 304 Å, respectively.
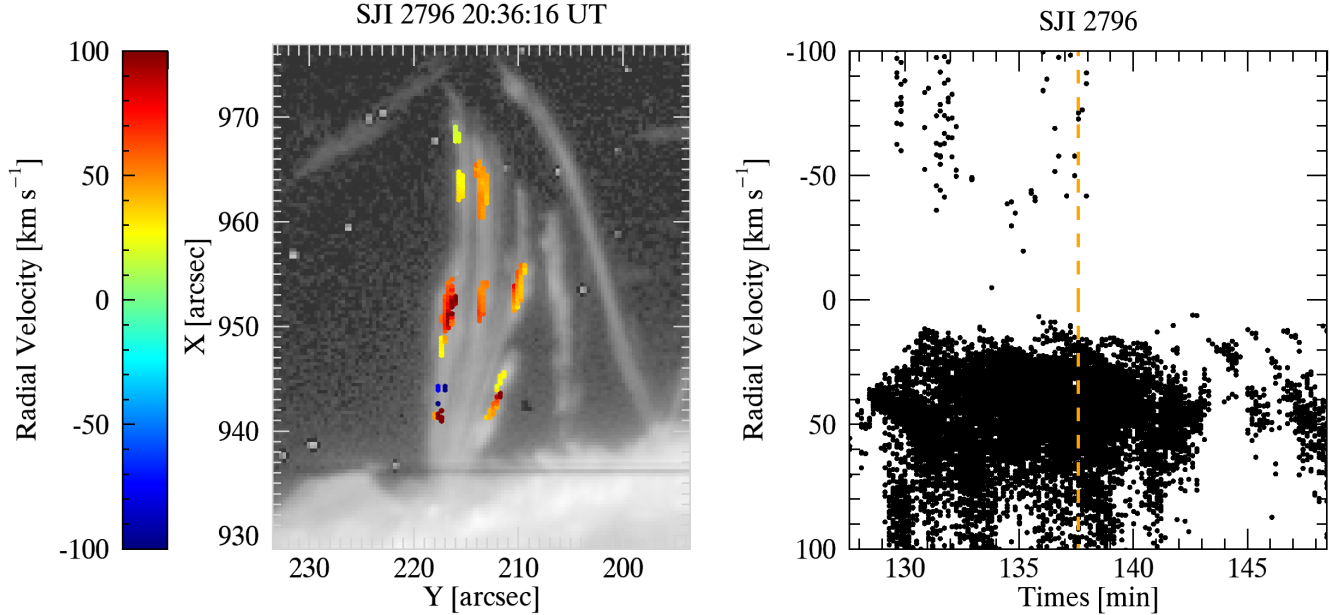


**Figure 10.** Left: One of the shower events observed in the SJI 2796 Å during the gradual phase. The coloured detected pixels show the radial velocity. Here, the positive values correspond to the downflow motions, while the negative values show the upflow motions. Right: The variation of radial velocity with the observational time. The orange dashed line indicates the time.

clearly seen in the middle bottom panels, the region filled with red-redish colours in the SJI 1330 Å map corresponds
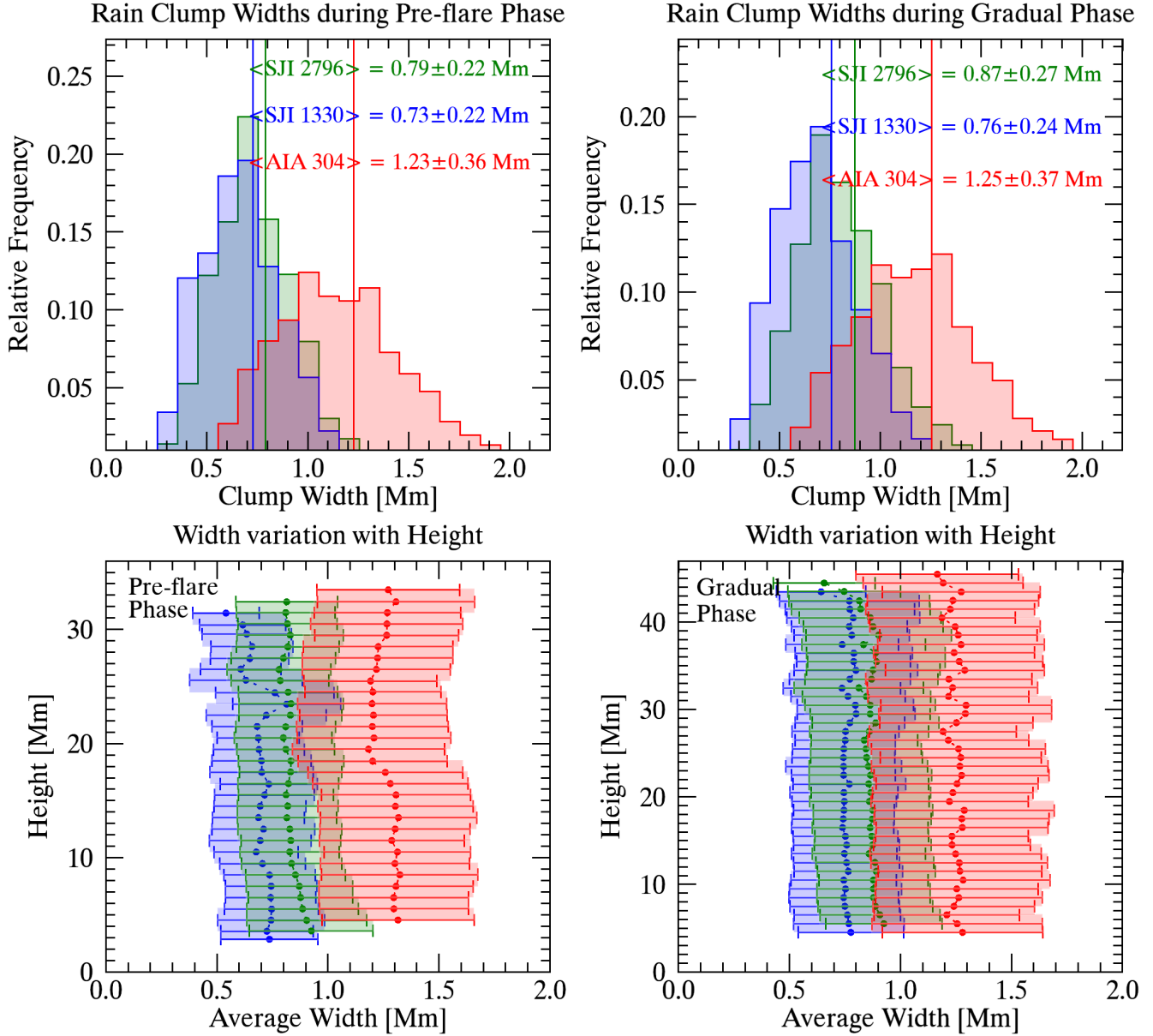
**Figure 11.** Top: Histograms of rain clump widths during the pre-flare (left) and gradual (right) phases. Green, blue and red denote SJI 2796 Å, SJI 1330 Å, and AIA 304 Å, respectively (see legend). Bottom: The width variation with projected height during the pre-flare (left) and gradual (right) phases. Here, the circles and error bars correspond to the median width and their standard deviation at each height bin.

to pixels within the CE region. We would like to note that there are many CE events in this region, and that is difficult to detect all of them because of the very diffuse emission. Therefore, here, we select two CE events in terms of their relative isolation. These two CE events are roughly indicated by small arrows in Figure 13. As expected, the SJI 2796 Å and Cool AIA 304 Å channels do not have any signature of these CE events.

We isolate and classify these pixels showing upflows in SJI 1330 Å during the impulsive phase as potential CE pixels (for the CE2) and plot the corresponding velocity map and histograms in Figure 14. Note that, in this plot, we released the conditions we used after the RHT routine to capture more material in the CE. We only include pixels for which $\overline{|\theta_t|} \leq 87°$ instead of $\overline{|\theta_t|} \leq 84°$. The maximum velocity extends to just over 400 km s$^{-1}$. We found that the average speed of CE is 139±83 km s$^{-1}$.
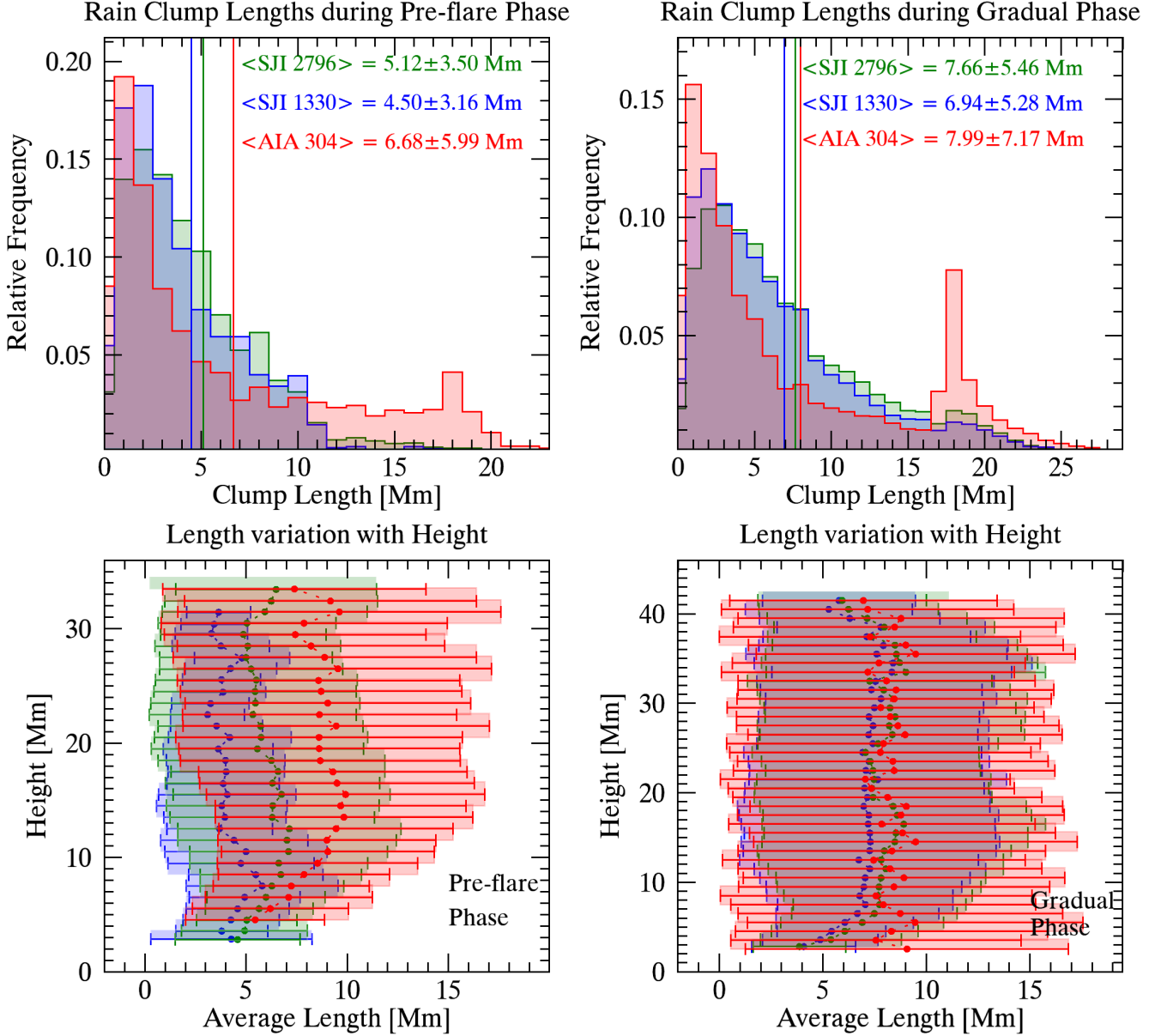
**Figure 12.** The same plots as shown in Figure 11 but for the length of rain clumps.

We have also tracked the CE events along the loop with the help of the CRisp SPectral EXplorer (CRISPEX) and Timeslice ANAlysis Tool (TANAT), two widget-based tools programmed in the Interactive Data Language (IDL). These tools provide easy browsing of the image or spectral data, the determination of loop trajectory, extraction, and further analysis of time-distance diagrams. Figure 15 shows the observed CE events in Fe XVIII and Fe XXI with the chosen and analyzed loop path (yellow dashed lines). On the right panels, we show time-distance (x-t diagram) maps obtained from the traced loop path on the left panels. The total time duration (see grey dashed lines in the x-t diagram) for the hot emission that accompanies CE1 and CE2 is roughly 33 and 44 min, respectively. However, this does not directly reflect the duration of each CE event. Indeed, besides CE, the hot emission can be produced by other sources, such as the work performed by the Lorentz force or directly from the reconnection region. To determine the true duration of the CE events we note the presence of bright emission propagating upwards from the footpoint, which last roughly 10 min and 19 min (see green dotted lines) for the CE1 and CE2, respectively. As we will see in section 4.3, this is corroborated by the SG analysis. We made multiple velocity measurements at different heights in these x-t diagrams, and we found a broad velocity distribution (see histogram plots) between 15 and 200 km s$^{-1}$, with
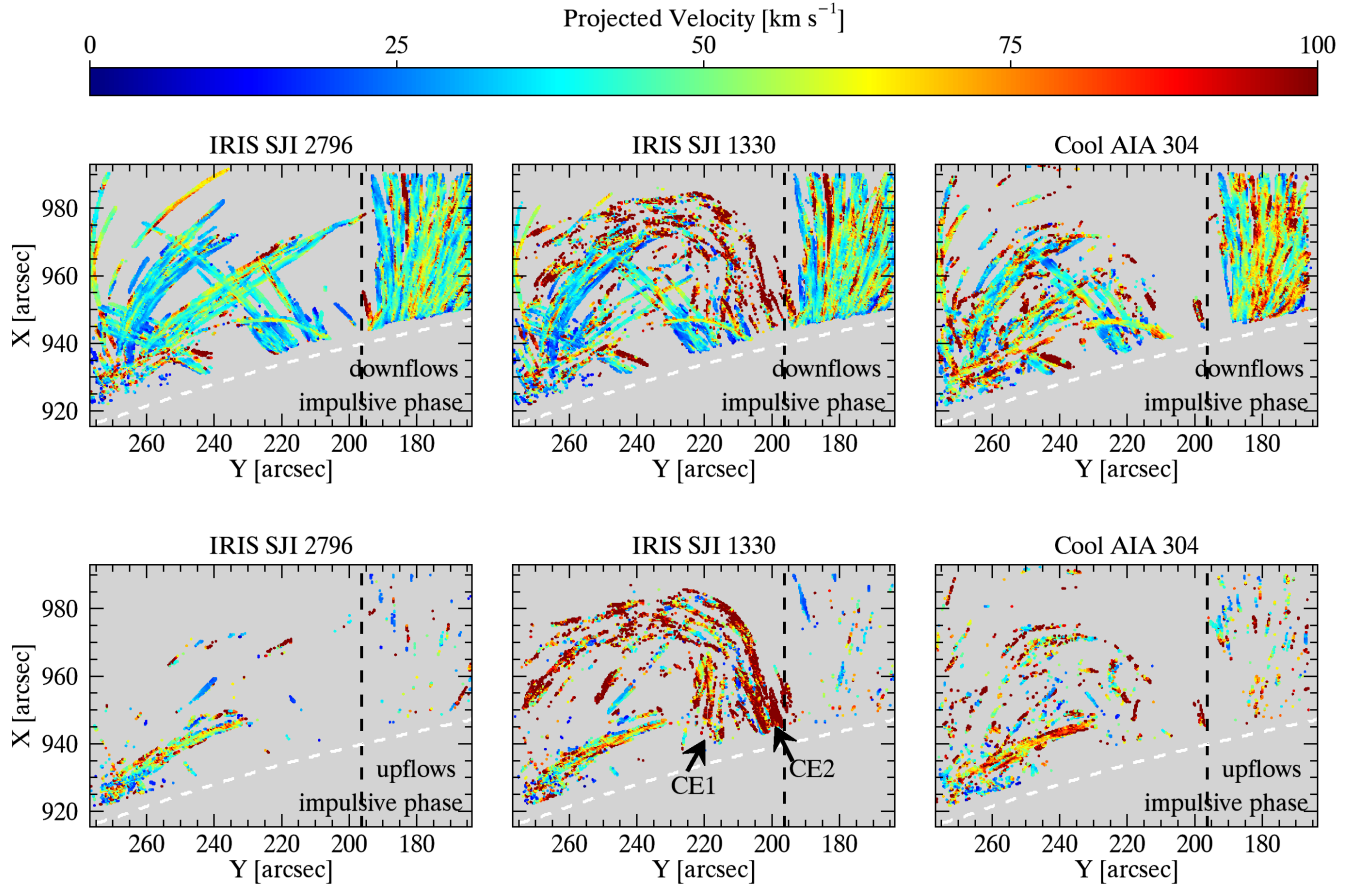
**Figure 13.** The same maps as shown in Figure 6 and Figure 7 but for the impulsive phase.
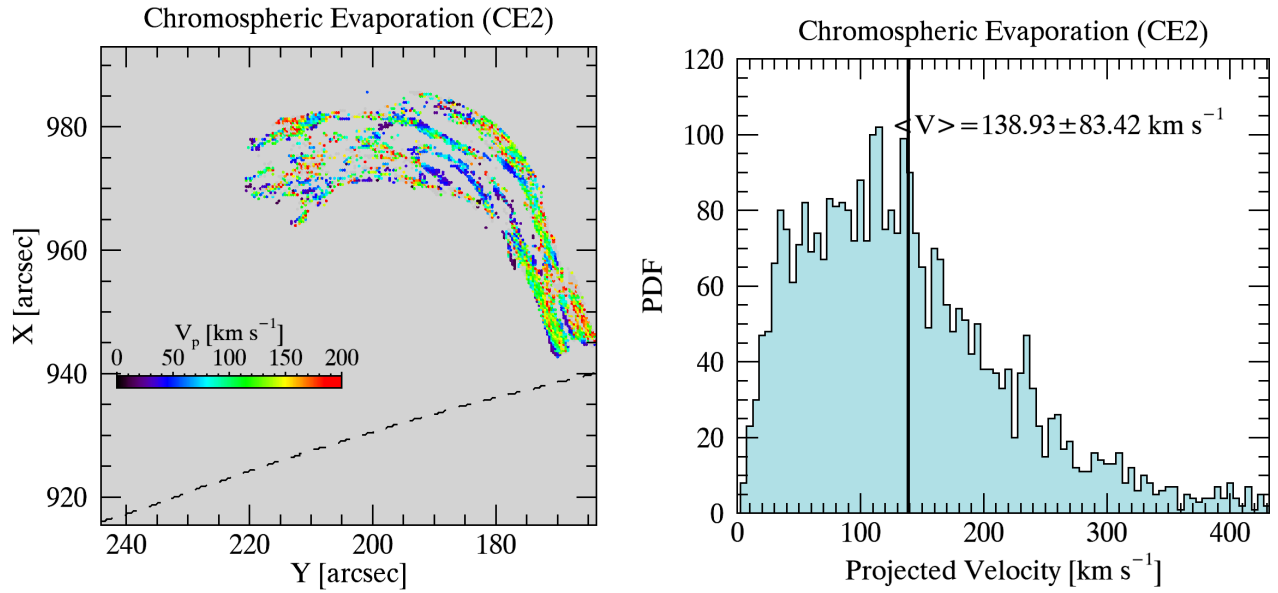


**Figure 14.** Left: Average upflow projected velocities of CE2 in SJI 1330 Å. Right: 1D velocity histogram distribution of the left panel.

an average 115±46 km s$^{-1}$ for the CE1. We found 136±32 km s$^{-1}$ on average for the CE2, which is consistent with the velocity from the RHT result.

### 4.2.2. *Chromospheric evaporation and rain shower morphology*

Here, we compare CE and flare-driven coronal rain to determine if the regions where we observe the rain shower align with those of CE. Figure 16 presents a composite image showing impulsive and gradual phases together. Here, the red and blue corresponds to the SJI 1330 Å and AIA 94 Å images, respectively, taken during the impulsive phase (19:30 - 20:25 UT), while the green is only taken from the SJI 2796 Å images in the time corresponding to the gradual phase (20:25 - 22:02 UT). A very fine intensity structure is seen in the CE, particularly in the SJI 1330 Å channel. This is further shown in the composite image by setting contours in brighter red for higher intensity.

Similar to the CE events, there are also many more shower events that likely correspond to CE events. We select two main shower events among all showers, namely SH1 and SH2 (see arrows in Figure 16), that seem to spatially correspond to the two previously selected CE regions, namely CE1 and CE2. In Figure 17, we show the CE1 region (left) observed during the impulsive phase and SH1 (right) during the gradual phase. The red and cyan colours show transverse cuts to the CE1 and SH1 events, taken at the same locations. The bottom panels in the same figure provide the time-averaged intensity over the distance of these coloured cuts, where the time intervals are those specified at the beginning of this section. The black line on these plots corresponds to the average intensity of these cuts. Similarly, Figure 18 shows the other CE and SH events: CE2 and SH2. Visual comparison of the overall morphology between CE and SH already reveals a strong similarity. We quantify this similarity by calculating their width. There are essentially two types of widths: an overall width for the entire (overall) CE or shower event (SH) and the strand width. To calculate the overall width, we fit a Gaussian over the intensity profile of the temporally summed image (see top and bottom panels in Figures 17 and 18, respectively) along each transverse cut (red and cyan) and set the width equal to the Full Width at Half Maximum (FWHM) of the Gaussian fit. In this process, we select the cuts (red and cyan) that are relatively isolated and do not intersect other neighbouring structures. We found that the width of the larger structure (i.e. the overall width) spans a range from [2294±55, 4813±208] km with 3872±104 km on average for the SH1 and [2771±83, 5825±163] km with 4088±107 km on average for the CE1. It is [2883±69,6869±270] km with 4427±157 km on average for the SH2 and [4634±82,6331±206] km with 5526±155 km on average for the CE2. These calculations are based on the average width measurements over the channel, and the overall average values for each channel (as shown in Figures A.1 and A.2) are given in Table 4 for each SH and CE event. Due to the high temperatures, the CE is only visible in certain channels. Also, the SH can be very dim in specific channels. Therefore, we have included only the channels for which the intensity values are larger than a specific noise threshold.

**Table 4.** Obtained overall width measurements for the SH and CE events across the channels.

|  | CE1 [km] | CE2 [km] | SH1 [km] | SH2 [km] |
|---|---|---|---|---|
| SJI 2796 | - | - | 3377±63 | 4318±231 |
| SJI 1330 | - | 5847±206 | 2950±59 | 6013±270 |
| Cool AIA 304 | - | - | 3313±59 | 3665±193 |
| AIA 171 | - | - | 3146±87 | 3584±143 |
| AIA 193 | - | - | 4126±115 | 4492±172 |
| AIA 211 | - | - | 4804±153 | 3216±123 |
| AIA 335 | - | 5293±82 | 4404±158 | - |
| AIA 94 | 5140±123 | 6331±201 | 4279±93 | 5663±137 |
| AIA 131 | 3036±90 | 4634±133 | 4454±147 | 4559±120 |

We also note the sub-structure within each event, which we refer to as CE strands or rain strands, accordingly. Because of the LOS superposition, the width of individual strands can appear much larger than their true value. Hence, for the width calculation, we select the thinnest strand over a particular time. As for the overall width, we fit a Gaussian intensity profile over a path crossing the strand transversely to the local trajectory, and retrieve the
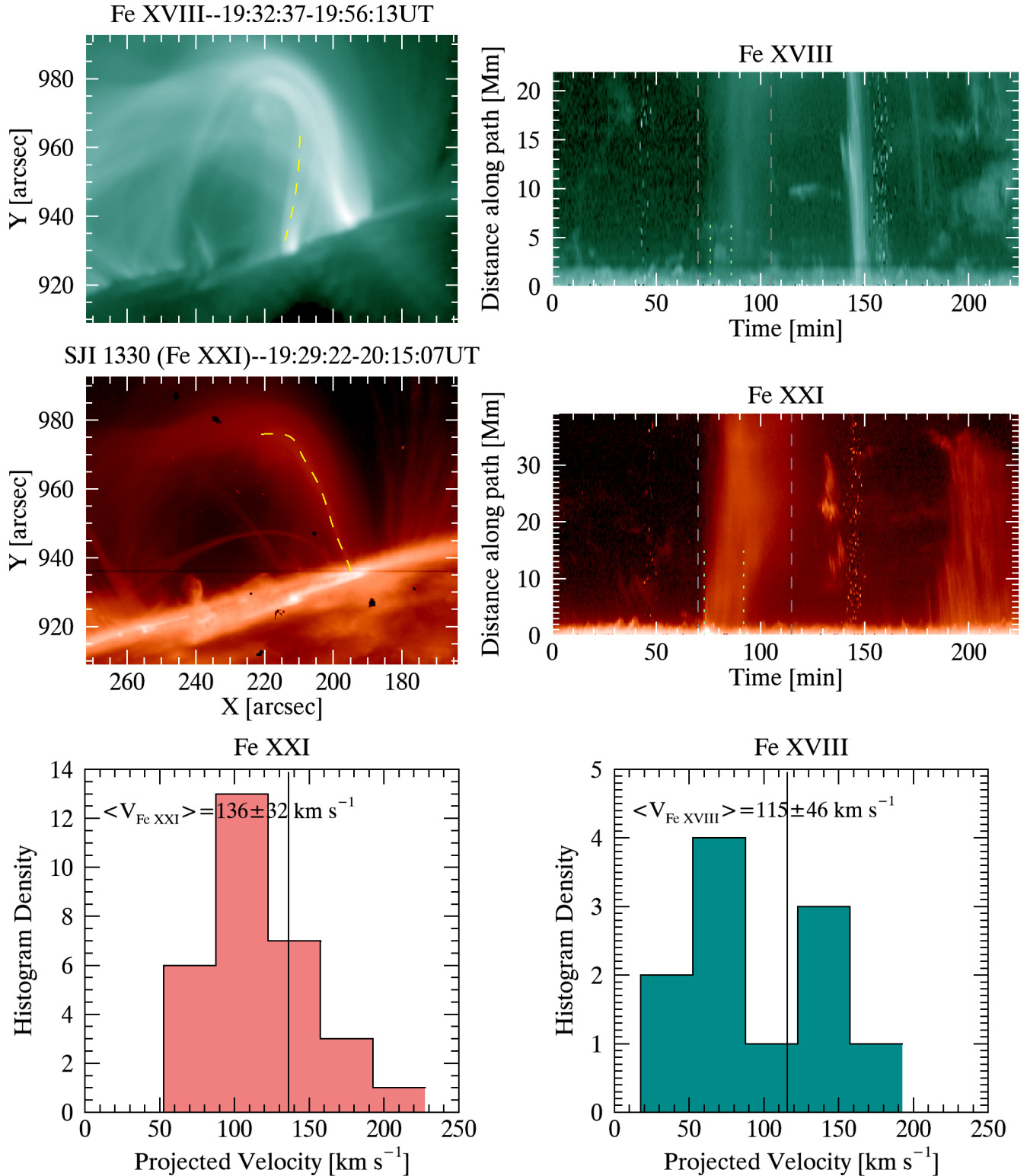
**Figure 15.** Observed CE1 (top-left) and CE2 (middle-left) regions, which are obtained by summing the images in the interval 19:32-19:56 UT and 19:29-20:15 UT during the impulsive phase in Fe XVIII and Fe XXI (SJI 1330), respectively. Yellow dashed lines in these panels correspond to the chosen and traced paths using the CRISPEX analysis tool. Their time-distance diagrams are shown in the right panels. The grey dashed lines indicate the total time duration of the hot emission in the respective channels, while the green dotted lines indicate the duration of the CE events. The bottom panels show the histograms for the calculated velocities with TANAT for the CE events. Solid vertical lines denote the mean values.
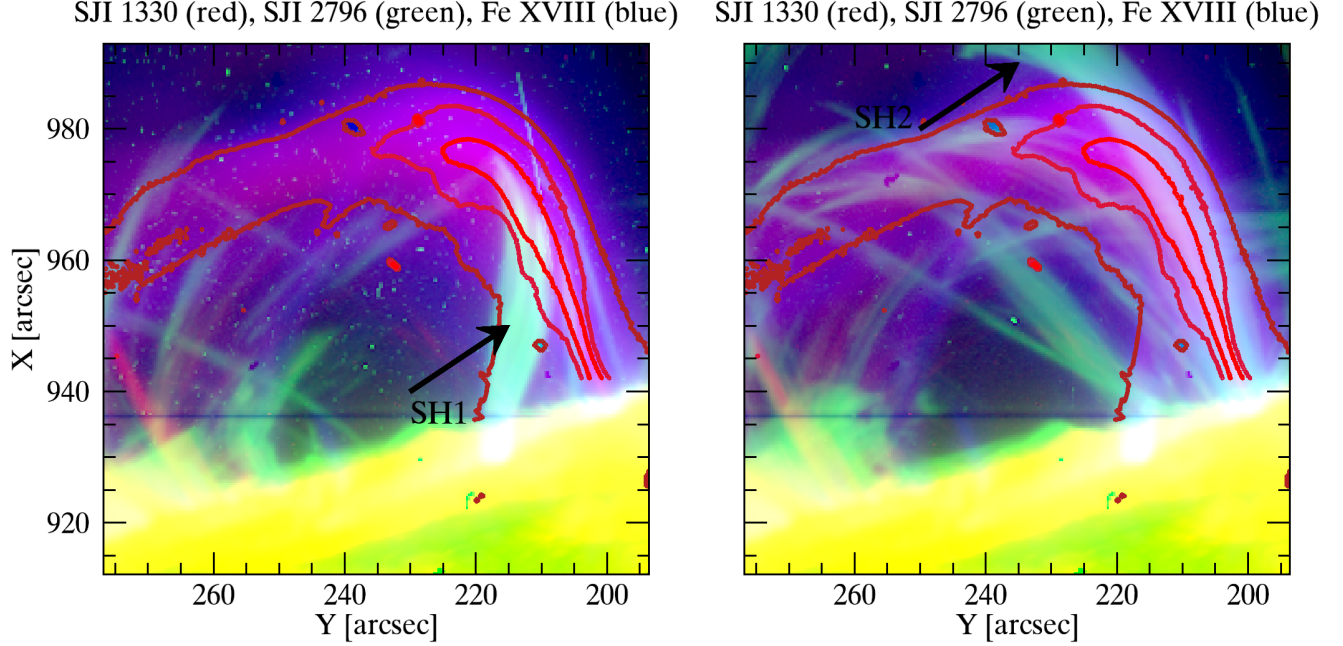
**Figure 16.** Composite image of the SJI 1330Å (red), SJI 2796Å (green), and Fe XVIII (blue) taken by different observational time range. The SJI 1330Å and Fe XVIII were obtained by summing the images in the interval 19:30 - 20:25. The SJI 2796Å results from images summed during the 20:25 - 20:37 UT (left) and 21:45 - 21:57 UT (right) interval. The contour lines are derived from the SJI 1330 Å, emphasizing the CE region based on the different intensity thresholds.

FWHM. We found that the average substructure width (i.e. strand width) is 642±56 km and 1218±176 km for the SH1 (based on the SJI 2796 Å) and CE1, respectively, while it is 720±145 km and 1534±37 km for the SH2 and CE2, respectively. These results suggest that there is a strong correspondence between shower events and CE in morphology at both sub-structure and larger structure levels.

### 4.3. *IRIS Spectra of the chromospheric evaporation*

To better constrain the properties of the CE and rain showers, we examine the Fe XXI, Mg II k and Si IV spectra obtained by IRIS. The left panels in Figure 19 show the spectra in the Fe XXI 1354.08 Å and Si IV 1402.77 Å lines of the CE1 and CE2 towards the start (UT19:36:52) along the part of the slit that covers the visible flare loop footpoint (red dashed vertical line in the SJI 1330 Å image of the top panel). In the Fe XXI spectra, we can see several localised intensity enhancements along the slit, which supports the presence of $10^7$ K plasma in both CEs. The enhanced level of emission across the wavelength range at around $195''$ corresponds to the ribbon location. At $200''$, we can see a stronger but more localised emission peak (intensity on the order of 10 DN), which corresponds to CE2. The width of the emission is only a few arcsec, which matches very well the CE width seen in the SJI in Figure 18. We plot over the spectral maps (wavelength vs slit axis) the spectral profiles at this specific point shown by the red diamond in the SJI figure (see caption for details). We fit with a single Gaussian the Fe XXI profile, and the best fit from a single or double Gaussian fitting of the Si IV 1402.77 Å profile. The profile is Doppler shifted towards the blue, with a value of -7±2.7 km s$^{-1}$, with a FWHM of 0.494 Å, which corresponds to 110±2.7 km s$^{-1}$. Taking a $10^7$ K peak formation temperature and taking into account the FUV instrumental width, we obtain a non-thermal line width of 25.8±2.7 km s$^{-1}$. On the other hand, the Si IV profile at this point shows a complex and very bright profile (>2000 DN) which is best fitted by a double Gaussian. The main component is relatively narrow (FWHM of 48.5±0.03 km s$^{-1}$) with almost no Doppler shift (1.69±0.03 km s$^{-1}$), and the second, dimmer component is broader (81.4±0.2 km s$^{-1}$) with a strong blue shift of -42.1±0.2 km s$^{-1}$. Assuming a peak formation temperature of $10^{4.8}$ for the Si IV line, we obtain non-thermal line widths of 20 km s$^{-1}$ and 34 km s$^{-1}$ for the main and secondary components, respectively, which are similar to those of the Fe XXI profile. This suggests that the flare heating giving rise to the CE2 is located below the formation height of the Si IV line (forming in the low TR), and pushes the TR plasma up, heating it to $10^7$ K. Further up the slit at $\approx 215''$, there is a wider spectral profile that belongs to CE1, about $5''$ in width, which
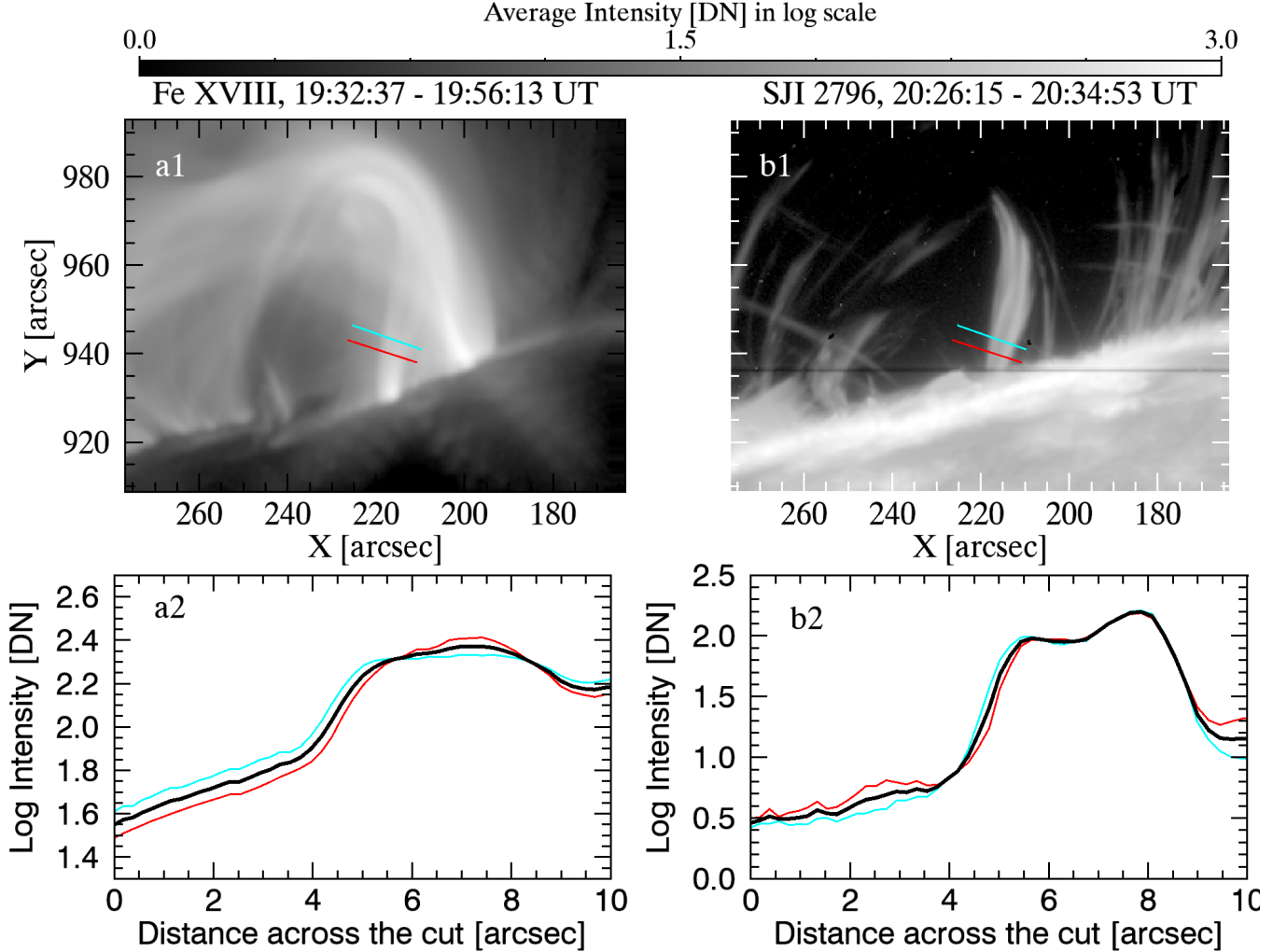
**Figure 17.** Top: Observed CE1 region during the impulsive phase in Fe XVIII (a1) and SH1 during the gradual phase in SJI 2796 Å (b1) in logarithmic scale. The red and cyan colours indicate the perpendicular cuts to the loop trajectory. Bottom: The intensity variation over the distance of these perpendicular cuts for the Fe XVIII (a2) and SJI 2796 (b2). Black curves show the average of these intensity variations.

has a redshift of 58.7±3.6 km s$^{-1}$ with a broad FWHM of 137±3.6 km s$^{-1}$, corresponding to a non-thermal line width of 43.7±3.6 km s$^{-1}$.

In Figure 20, we show statistics of the spectral fitting results of the Fe XXI line along the slit (top panel) and over time (bottom panel). We choose to remove the location corresponding to the ribbon to focus on both CEs instead. We also pose a relatively large threshold for the peak intensity of the profile of 5 DN (with the background noise at ≈ 2 DN). We can identify CE1 between 212″and 219″(green points in the figure), whose spectral signatures can be detected for 14 min, and CE2 around 201″ up to 205″or so (red points in the figure), which lasts 10 min. The widths closely match the overall widths of the CEs seen in SJI, shown in Figures 17 and 18. Furthermore, we observe strong variations in speed on the order of 1 − 2″, which matches the widths of the substructures seen in the SJI. The duration for both CEs is significantly shorter than the total duration of the hot emission seen in the SJI, but match the duration over which we see the upward propagating features from the footpoint in the SJI (see x-t diagrams in Figure 15), thereby confirming our previous interpretation that the CEs duration is short. It is nonetheless possible that further CE is happening at these locations, but is too faint to be observed with the SG instrument. Indeed, we note that both CEs have low Fe XXI intensities, between 10 DN and 20 DN, and our intensity threshold is set rather high. Regarding the dynamics, CE1 exhibits a strong red shift up to 190 km s$^{-1}$, with an average of 40 km s$^{-1}$ and a standard deviation
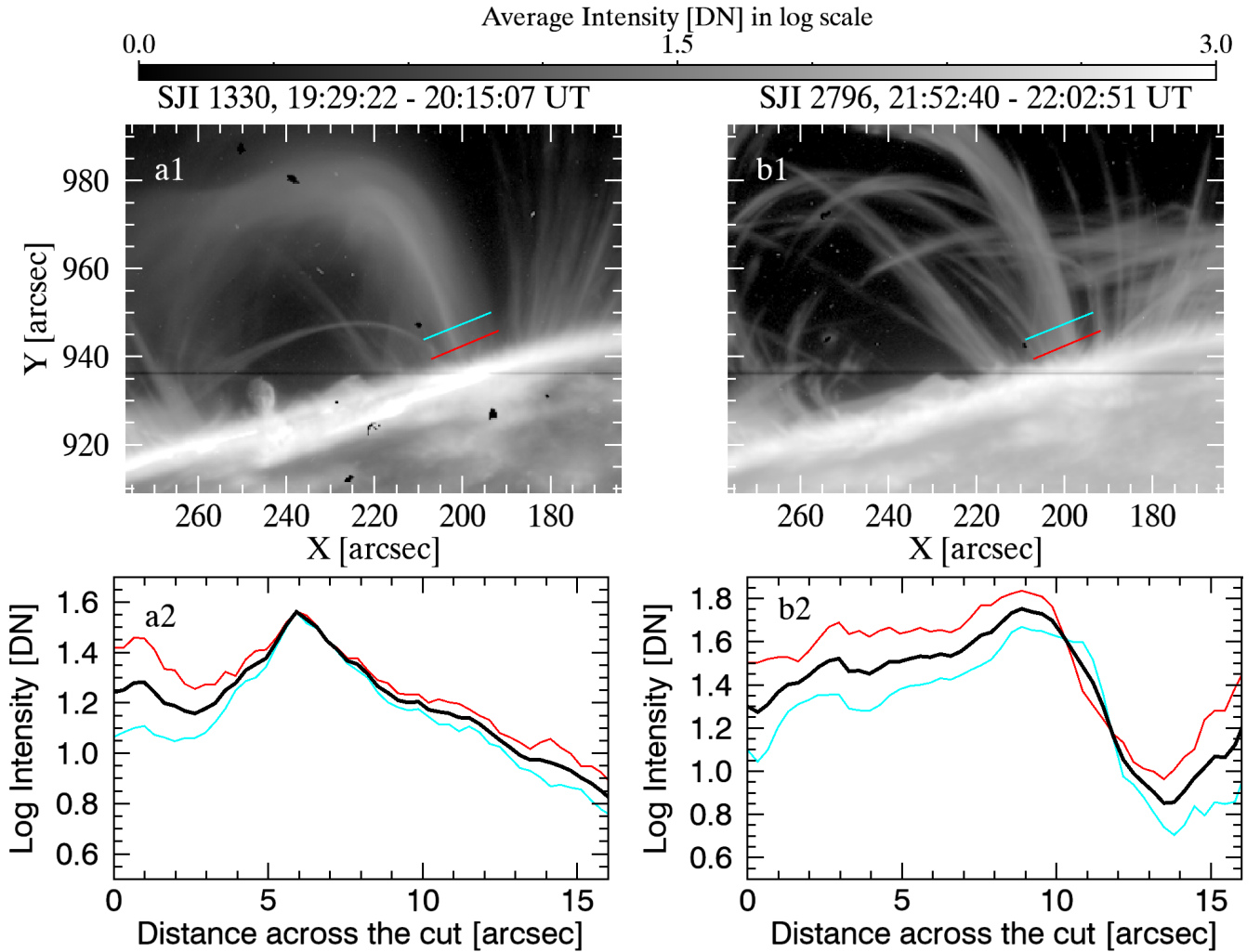
**Figure 18.** Top: Observed CE2 region during the impulsive phase in SJI 1330 Å (a1) and SH2 during the gradual phase in SJI 2796 Å in logarithmic scale. The red and cyan colours indicate the perpendicular cuts to the loop trajectory. Bottom: The intensity variation over the distance of these perpendicular cuts for the SJI 1330 (a2) and SJI 2796 (b2). Black curves show the average of these intensity variations.

of 31 km s$^{-1}$. The non-thermal velocities are relatively small, with an average of 28 km s$^{-1}$ and a standard deviation of 13 km s$^{-1}$. On the other hand, CE2 shows a strong, more localised, blue shift at $\approx -60$ km s$^{-1}$, with an average of 26 km s$^{-1}$ and a standard deviation of 37 km s$^{-1}$. The non-thermal velocities of CE2 are significantly larger than those of CE1, with a maximum up to 184 km s$^{-1}$, an average of 73 km s$^{-1}$ and a standard deviation of 36 km s$^{-1}$. The difference in the Doppler shift extrema and average non-thermal velocities between both CEs suggests a difference in the magnetic field topology with respect to the LOS, and also the presence of magnetic shear and unresolved structure at the loop footpoint.

The temporal evolution of CEs shows a rapid decrease in both Doppler and non-thermal velocities for CE1, but only a decrease in non-thermal velocity for CE2, with the fast values lasting less than 2 min for CE1 and $\approx 5$ min for CE2. This suggests a transition from explosive to gentle evaporation. The duration of the fast and gentle velocity phases are consistent with previous reports (Fletcher et al. 2013; Sellers et al. 2022). The decrease in the non-thermal velocity for CE2 occurs without a significant decrease in the Doppler velocity, suggests the presence, and corresponding reduction, of turbulence (Polito et al. 2019).

One question is whether the observed POS speeds with SJI are a good measure of the total speeds. The spectra reveals large Doppler and non-thermal velocities but highly localised in space and in time. As mentioned above, this

suggests the presence of magnetic shear and unresolved structure at the footpoint. This would suggest that the POS velocities measured higher up are not far from the total velocity values. However, we can calculate an upper bound estimate $v_{tot} = \sqrt{v_{POS}^2 + v_{LOS}^2}$ taking as the LOS component $v_{LOS}$ the largest value between the average Doppler velocity and the non-thermal velocity for each CE. This gives total velocities of $122 \pm 38$ km s$^{-1}$ and $154 \pm 33$ km s$^{-1}$ for CE1 and CE2, respectively.

### 4.4. IRIS Spectra of the rain shower

We now analyse the spectra of the rain showers. Because of the very low location in height of the slit, we can only properly detect the spectroscopic features of SH1. Indeed, we could not find any Doppler signature for SH2, in neither the Mg II nor Si IV lines. It is possible that because of the small shift in location introduced by the solar rotation (due to West limb location of event and SH2 occurring 130 min after CE2), the slit at that location has shifted too low in height for the rain to be observed. Since the slit is higher up for SH1, the effect of solar rotation is less pronounced.

In the right panels of Figure 19, we show the map for the Mg II k line (middle panel) and Si IV line (bottom panel) for a snapshot during SH1. We can see the blue-shifted rain as it falls and we select a point in SH1 (red diamond in the SJI image) and overlay the corresponding profile over the spectral maps. In this case, double Gaussian fits provide the best fits for both Mg II k and Si IV spectra. For Mg II k, we obtain a Doppler shift of $13.85 \pm 0.06$ km s$^{-1}$ and $-35.05 \pm 0.075$ km s$^{-1}$. The corresponding non-thermal line width (assuming a formation temperature of $10^4$ K for Mg II k and including the instrumental width for the FUV) is $13.20 \pm 0.0075$ km s$^{-1}$ and $33.54 \pm 0.06$ km s$^{-1}$. For Si IV, both components are blue-shifted, with $-12.73 \pm 0.25$ km s$^{-1}$ and $-63.13 \pm 0.37$ km s$^{-1}$, and corresponding non-thermal line widths of $15.05 \pm 0.25$ km s$^{-1}$ and $33.20 \pm 0.37$ km s$^{-1}$. We note that the non-thermal line widths are very similar between both lines (as expected for coronal rain), while the Doppler velocities are not. It is likely that the Mg II profiles suffer from large optical thickness, thereby affecting the measured Doppler velocities. We can therefore assume that the real Doppler velocity of the rain is the most blue-shifted component of Si IV.

Figure 21 shows the spatial (top panel) and temporal (bottom panel) distribution of the spectral line fitting for the Si IV line. We focus on SH1 (for the reasons explained above) by selecting the slit range determined by the Fe XXI results, that is, between $211''$ and $220''$. We also limit the results to a time range that contains the interval over which the SH1 is seen to cross the slit in the SJI, and also before the occurrence of the cosmic ray episode (see Figure 5). The appearance of the rain is clear in the Doppler velocity temporal distribution, where the appearance of a strong blue shifted component is continuously seen from $\approx 132$ min. The maximum blue shifted value is $-138$ km s$^{-1}$. We obtain an average Doppler velocity for the Doppler shifted component (corresponding to the rain) of $-56$ km s$^{-1}$ with a standard deviation of 18 km s$^{-1}$. The corresponding average non-thermal velocity is 30 km s$^{-1}$ with a standard deviation of 8 km s$^{-1}$. We note that the combined dynamics from the average Doppler and non-thermal velocities of the SH1 and CE1 are very similar in magnitude. The fact that the non-thermal velocity of the SH1 is smaller than that of CE1 supports the presence of turbulence and/or unresolved emission at faster speeds for the CE (as observed in the POS component). As done for the CE, we can provide an upper bound for the total average velocity for SH1 taking the average Doppler velocity into account. We obtain $v_{tot} = 83 \pm 16$ km s$^{-1}$.

### 4.5. Mass-flux analysis

#### 4.5.1. Energetics and Thermodynamics of Chromospheric Evaporation

We investigate the mass and energy cycles during the impulsive phase. As we mentioned, we have two main CEs (CE1 and CE2) at different times. We first applied the DEM method based on the "simreg" technique (Plowman & Caspi 2020) and obtained the emission measure (EM) for each temperature bin, starting from $\log T = 5.5$ to 7.2 for each CE. Figure 22 displays two EM maps corresponding to the temperature bins of $\log T = 6.9 - 7.0$ (on the left) and $\log T = 7.1 - 7.2$ (on the right). These temperature ranges exclusively encompass instances where CE is observed. We defined sub-regions in the respective temperature bins (see Figure 22) marked by white rectangles for both CE1 and CE2. To define these sub-regions, we intentionally excluded footpoints due to the presence of the solar disc. Our analysis commences by calculating the average EM variations for both temperature bins and for each CE event across distinct time intervals derived from SG analysis. The time interval for the $\log T = 6.9 - 7.0$ and $\log T = 7.1 - 7.2$ bin extends from 19:35:07 to 19:49:19 ($\Delta t \approx 14$ min). In the case of CE2, these bins encompass the period from 19:35:31 to 19:45:55 ($\Delta t \approx 10$ min).
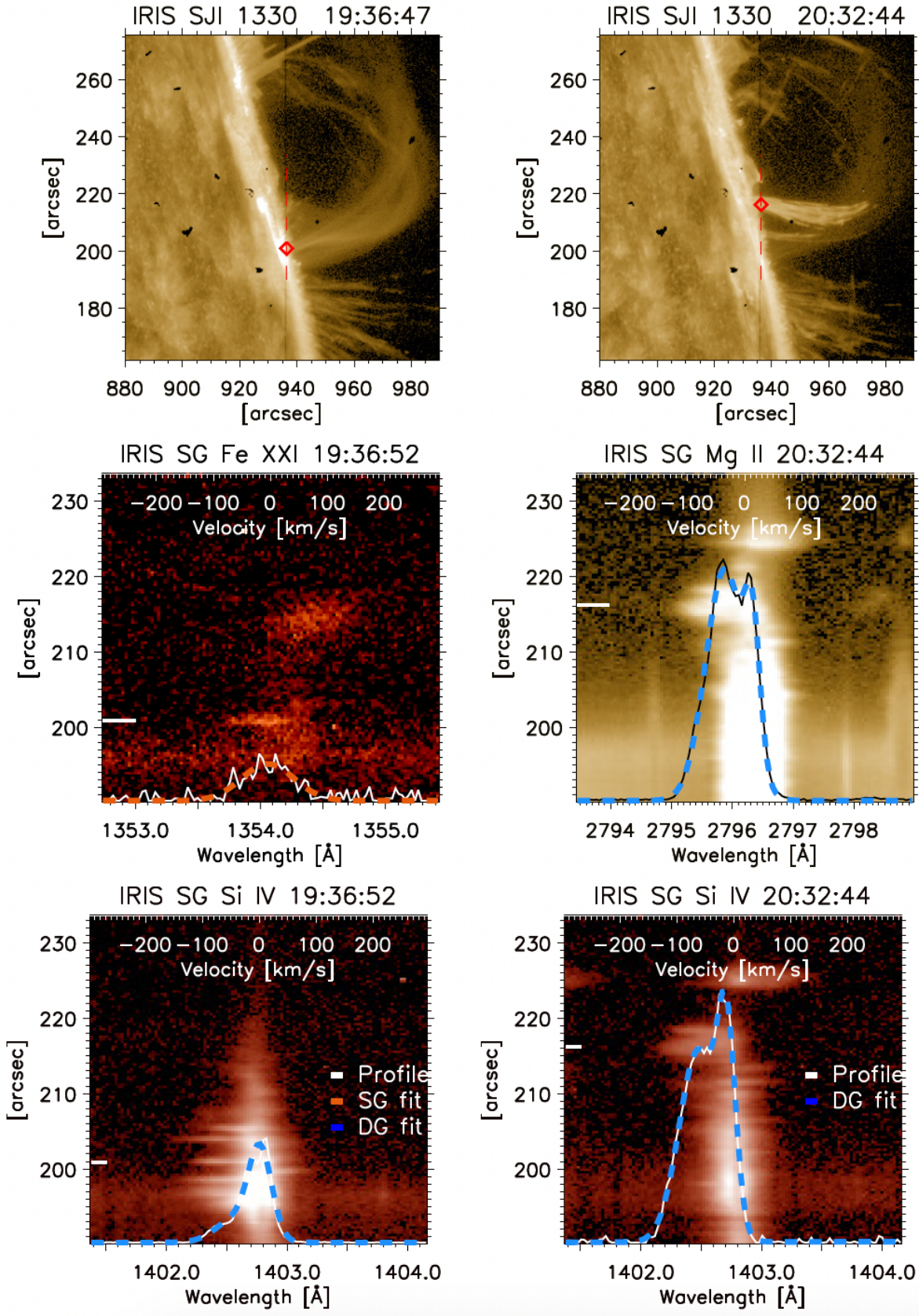
**Figure 19.** IRIS 1330 Å spectra for the CE (including both CE1 and CE2, left panels) and SH1 (right panels) (time is indicated at the top of each panel). The vertical red dashed lines in the IRIS/SJI panels show the portion of the IRIS/SG slit shown in the spectral maps of the Fe XXI (middle left), Mg II (middle right) and Si IV (bottom row) lines. The overlaid line profiles in the maps (white curves) correspond to the positions marked by the red diamonds in the SJI images, corresponding to the location of the slit in the spectral maps indicated by the short horizontal white lines on the left. The spectral profiles are fitted with either a single ('SG', dashed orange curve) or a double ('DG', dashed blue curve) Gaussian.
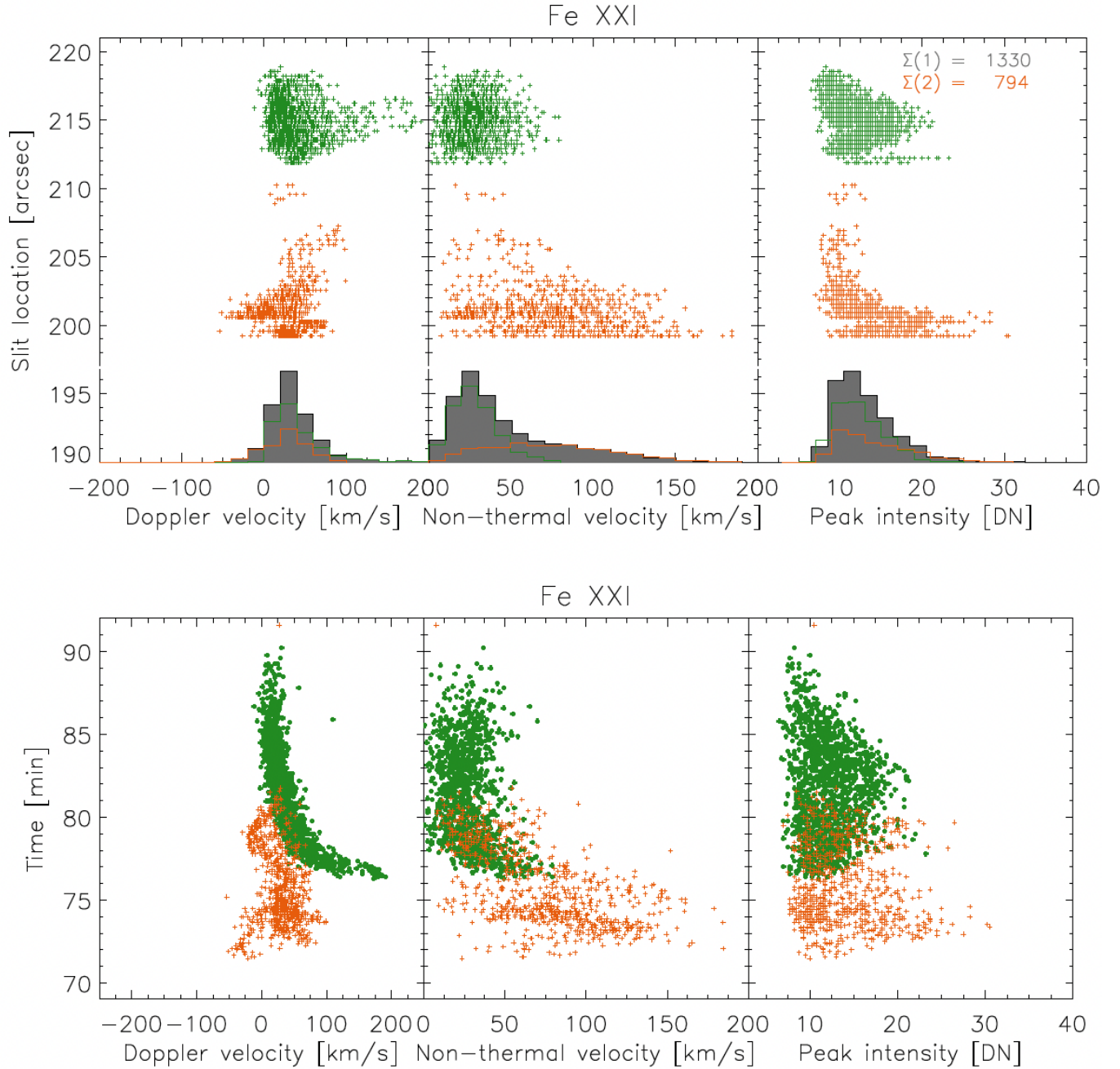
**Figure 20.** Spatial and temporal distribution of the Fe XXI 1354.08 Å spectra. We select spectral line profiles satisfying specific requirements (see section 3) and fit them with a single Gaussian. We restrict the slit range between $199''$ and $220''$ to focus on CE1 (green points) and CE2 (orange points). From the Gaussian fitting we obtain the Doppler velocity (left panels), non-thermal velocity (middle panels, obtained by subtracting the instrumental line width and the thermal component taking the peak formation temperature for the line), and the peak intensity (right panels). The spatial and temporal distribution are shown in the top and bottom rows, respectively. We also show the histograms of the distribution for each quantity on the top row, with the total in grey, and the green and orange outline histograms for the CE1 and CE2, respectively. The sum of points for each CE is shown on the top right panel with the respective number.
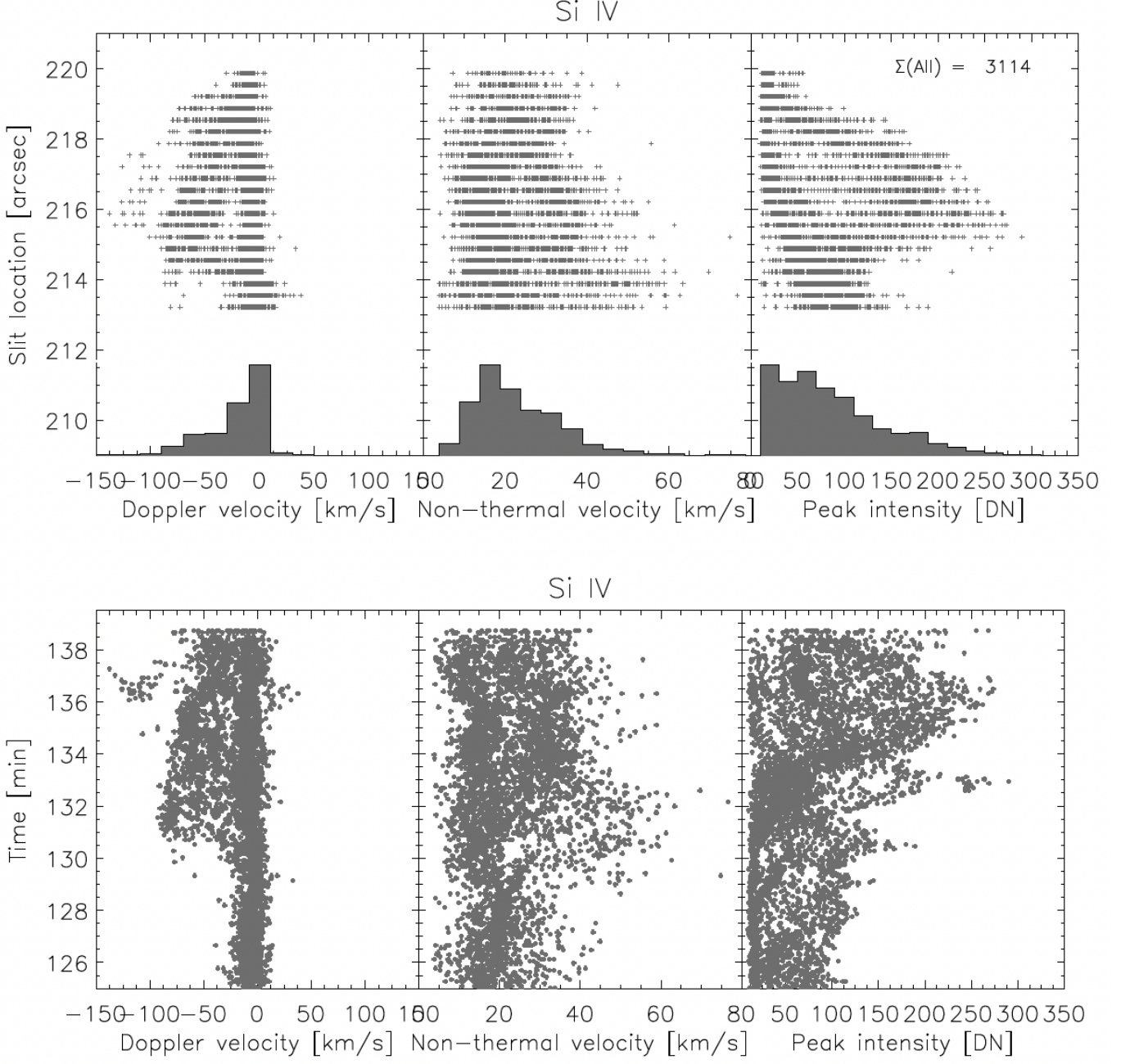
**Figure 21.** Spatial and temporal distribution of the Si IV 1402.77 Å spectra. Similar to Figure 20 for the Si IV line, and we focus only on SH1 by restricting the slit range between 211″and 220″(as seen from Figure 20) and the time range over which SH1 is observed (and avoiding the cosmic ray episode, see Figure 5). The best fit is selected from a single or double Gaussian. The sum of all points is shown on the top right panel.

We take the temperature of the CE $T_{CE}$ to be the average DEM-weighted temperature ($\overline{T}_{DEM}$), which is calculated using the Equation 10:

$$\overline{T}_{DEM} = \frac{\int (DEM(T) - DEM(T)_{t_0}) \times T dT}{\int (DEM(T) - DEM(T)_{t_0}) dT}$$

$$T_{CE} = \overline{T}_{DEM},$$

(10)
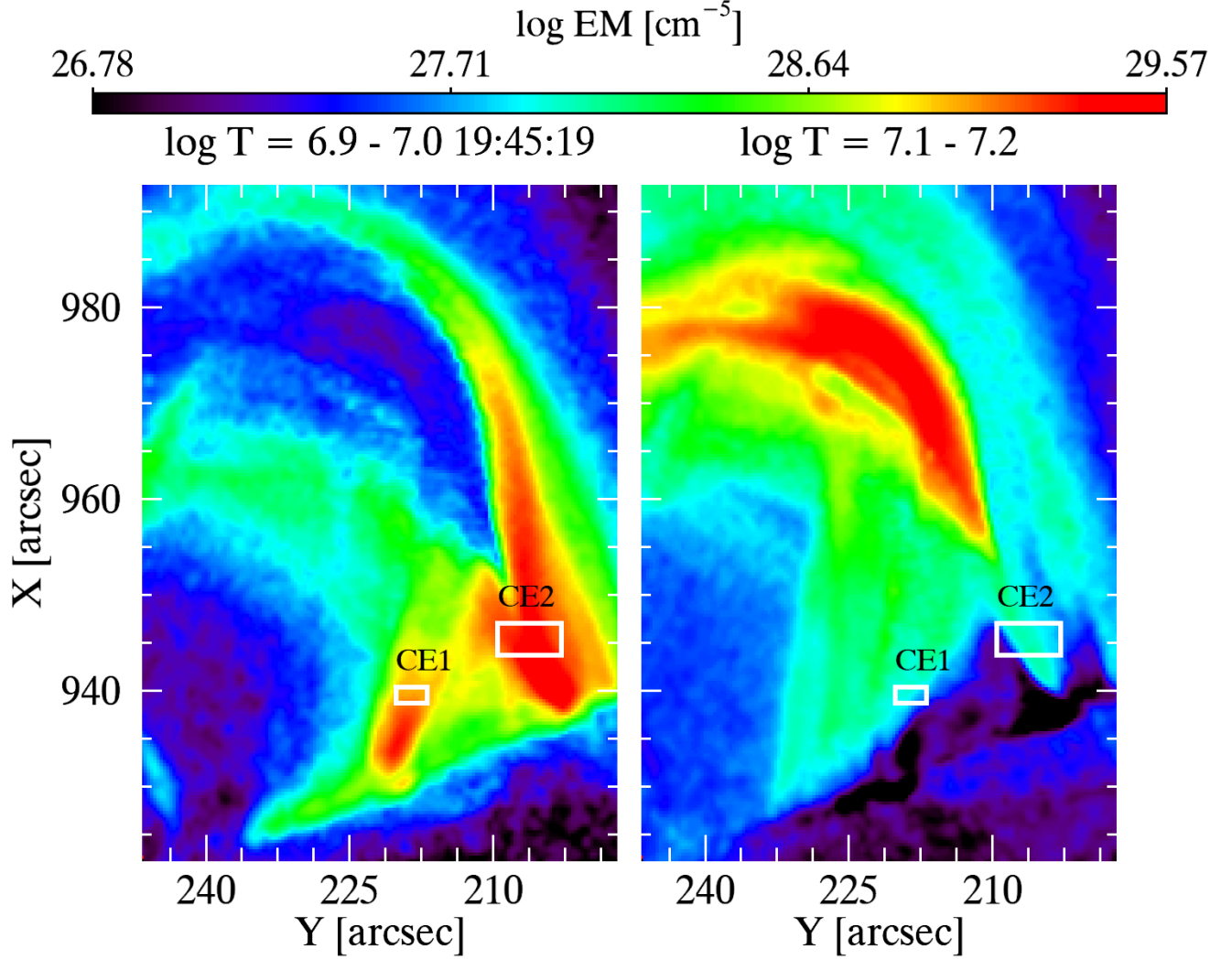
**Figure 22.** EM maps for the $\log T = 6.9 - 7.0$ (left) and $\log T = 7.1 - 7.2$ (right). The white rectangle areas show the focused region within the CE1 and CE2 for the detailed mass-flux analysis.

where the integral is performed exclusively over the two temperature bins where the CE1 and CE2 are observed. Here, $t_0$ denotes a time immediately prior to the occurrence of the CE. However, $DEM(T)_{t_0} = 0$ in this case, since no emission in the hot bins is seen prior to CE. We find $T_{CE} = [8.95 \pm 3.28] \times 10^6$ K and $[8.62 \pm 3.28] \times 10^6$ K for CE1 and CE2, respectively.

Then, the average $EM$ over these temperature bins is given by $\Delta EM$ from Equation 11.

$$\Delta EM = \int (DEM(T) - DEM(T)_{t_0}) dT, \tag{11}$$

where $DEM(T)_{t_0} = 0$ for CE. The average $EM$ is found to be $[1.86 \pm 1.55] \times 10^{28}$ cm$^{-5}$ for the CE1 and $[6.55 \pm 3.93] \times 10^{28}$ cm$^{-5}$ for the CE2. With the help of these findings, we then calculate the total number density ($n_{CE}$) and mass density ($\rho_{CE}$) of the CE as follows:

$$
\begin{aligned}
n_{DEM} &= \sqrt{\frac{1.2 \times EM}{w_{overall}}} \\
n_{CE} &= 1.92 n_{DEM} \\
\rho_{CE} &= 1.17 n_{DEM} m_p,
\end{aligned}
\tag{12}
$$

where $n_{DEM}$ denotes the electron number density and where we have assumed a 10% Helium abundance, a fully ionised plasma and $m_p$ is the proton mass. Although we observe substructure within the CE, the internal structure (for instance, if composed of individual strands), is unclear. Hence, we take $w_{overall}$ as the observed overall width of the CE. To estimate the density of the CEs we focus on the observed strands. We find a strand mass density of $\rho_{CE} = [1.44 \pm 0.02] \times 10^{-14}$ g cm$^{-3}$ for the CE1 and $[2.33 \pm 0.03] \times 10^{-14}$ g cm$^{-3}$ for the CE2. Then, we calculate the mass rate ($R_{tot}$), the mass flux ($F_{tot}$), and the total mass $M_{to}$ for each CE according to:

$$R_{tot} = \rho A v_{tot}$$
$$F_{tot} = \rho v_{tot} \tag{13}$$
$$M_{tot} = R_{tot} \times \Delta t$$

Here, the CE total velocity is given by $v_{tot}$, the cross-sectional area $A$ of the CE is $A_{CE} = \pi r^2$, assuming a cylinder, and the mass density $\rho = \rho_{CE}$ for the CE. We use the upper bound for the total velocity found by combining the SJI and SG measurements, $[122 \pm 38]$ km s$^{-1}$ for CE1 and $[154 \pm 33]$ km s$^{-1}$ for CE2. The mass rate ($R_{tot}$) and the mass flux ($F_{tot}$) are found to be $[2.31 \pm 0.01] \times 10^{10}$ g s$^{-1}$ and $[1.76 \pm 0.01] \times 10^{-7}$ g cm$^{-2}$ s$^{-1}$, respectively, for the CE1. These are $[8.61 \pm 0.03] \times 10^{10}$ g s$^{-1}$ and $[3.59 \pm 0.08] \times 10^{-7}$ g cm$^{-2}$ s$^{-1}$, respectively, for the CE2. Given the $\Delta t = 14$ min and 10 min duration of CE1 and CE2, the total mass going into the loop is $M_{tot} = [1.94 \pm 0.01] \times 10^{13}$ g and $[5.16 \pm 0.02] \times 10^{13}$ g, respectively. The kinetic energy ($E_k$) is given by:

$$E_k = \frac{1}{2} \rho v_{tot}^2 V$$
$$V = A v_{tot} \Delta t. \tag{14}$$

For the CE we take the mass density $\rho = \rho_{CE}$, volume $V = V_{CE}$ and cross-sectional area $A = A_{CE}$. We find that the kinetic energies are $[1.44 \pm 0.02] \times 10^{27}$ erg for the CE1 and $[6.12 \pm 0.05] \times 10^{27}$ erg for the CE2. Finally, the thermal energy ($E_{th}$) is given by:

$$E_{th} = \frac{3}{2} n k_B T V, \tag{15}$$

where for the CE we take the total number density $n = n_{CE}$, temperature $T = T_{CE}$ and volume $V = V_{CE}$, with $k_B$ the Boltzmann constant. We find thermal energies ($E_{th}$) of $[3.54 \pm 0.01] \times 10^{28}$ erg and $[9.06 \pm 0.03] \times 10^{28}$ erg for the CE1 and CE2 events, respectively. Then, the total energy ($E_{tot} = E_k + E_{th}$) is $[3.68 \pm 0.02] \times 10^{28}$ erg for the CE1 and $[9.67 \pm 0.03] \times 10^{28}$ erg for the CE2. A summary of all these calculations is given in Table 5.

In addition to these, we also estimate the total thermal energy of the flare via Equation 15, with $T = \overline{T}_{DEM} = 9 \times 10^6$ K considering the emission measure over the respective duration of the hot emission accompanying each CE event. Also, the volume in this case is that of the flare loop where we see the hot emission. For this measurement, we find the total number density ($n_{DEM}$) to be $1.91 \times 10^{10}$ cm$^{-3}$. By approximating the loop to a box, we estimate the volume using $V = w^2 L$, with $L$ (62.5 Mm) the length of the flare loop, and $w$ (18.3 Mm) the observed width, which we assume roughly equal to the depth. We find that the total thermal energy of the flare is roughly $7.52 \times 10^{29}$ erg.

### 4.5.2. *Energetics and Thermodynamics of Flare-driven Coronal Rain*

Similar to CE, we also examine the mass and energy flow during two shower events observed at different times, which we previously named SH1 and SH2. SH1 event starts at 20:26:31 UT and ends at 20:35:31 UT, while the SH2 is between 21:18:31 and 21:46:43 UT. We show emission measure (EM) maps of these two shower events for each temperature bin in Figures 23 and 24. Contrary to the CE case, the rain, being multi-thermal, its $EM$ spans many temperature bins. We define as 'warm rain' the plasma emitting in the temperature bins above $\log T = 5.5$ (where the material is certainly optically thin), and 'cool rain' as the material below these temperatures (including the chromospheric range). A further difference with the CE is that prior to the rain occurrence, the $EM$ is significant across the temperature range. Hence, in these maps, we remove the $EM$ value immediately prior to the occurrence of the showers, at $t_0$ =20:26:19 for the SH1 and $t_0$ =21:18:19 for the SH2. This is to remove the strongly emitting background and capture as close as possible the $EM$ from the showers themselves.

**Table 5.** Measurements of the CE and SH events. For CE1, CE2, SH1, and SH2 we show the following quantities: duration ($\Delta t$), POS, LOS, and total velocity ($v_{POS}, v_{LOS}, v_{tot}$), strand and overall width ($w_{strand}$ and $w_{overall}$), average emission measurement ($<EM>$), mass rate ($R_{strand}$), mass flux ($F_{strand}$), total mass rate ($R_{tot}$), total mass flux ($F_{tot}$), strand and total mass ($M_{strand}$ and $M_{tot}$), kinetic energy ($E_k$), thermal energy ($E_{th}$) and total energy ($E_{tot} = E_k + E_{th}$). We also show temperature ($T$), total number density ($n$), and mass density ($\rho$), with the sub-index $CE$ or $rain$ depending on the case. The sub-indexes $cool$, $warm$ denote the cool and warm components of the rain. $N_{strand}$ corresponds to the minimum number of rain strands.

| | CE1 | CE2 | SH1 | SH2 |
|---|---|---|---|---|
| $\Delta t$ [min] | 14 | 10 | 9 | 28 |
| $v_{POS}$ [km s$^{-1}$] | [115±39] | [136±32] | [61±14] | [76±12] |
| $v_{LOS}$ [km s$^{-1}$] | [40±31] | [73±36] | [56±18] | - |
| $v_{tot}$ [km s$^{-1}$] | [122±38] | [154±33] | [83±16] | [76±12] |
| $w_{strand}$ [km] | [1218±176] | [1535±37] | [642±56] | [720±145] |
| $w_{overall}$ [km] | [4088±107] | [5526±155] | [3872±104] | [4427±157] |
| $<EM>$ [cm$^{-5}$] | $[1.86 \pm 1.55] \times 10^{28}$ | $[6.55 \pm 3.93] \times 10^{28}$ | $[1.52 \pm 0.67] \times 10^{27}$ | $[1.29 \pm 0.38] \times 10^{27}$ |
| $T_{CE}$ [K] | $[8.95 \pm 3.28] \times 10^6$ | $[8.62 \pm 3.28] \times 10^6$ | - | - |
| $n_{CE}$ [cm$^{-3}$] | $[1.42 \pm 0.02] \times 10^{10}$ | $[2.29 \pm 0.03] \times 10^{10}$ | - | - |
| $\rho_{CE}$ [g cm$^{-3}$] | $[1.44 \pm 0.02] \times 10^{-14}$ | $[2.33 \pm 0.03] \times 10^{-14}$ | - | - |
| $T_{warm}$ [K] | - | - | $[4.09 \pm 0.59] \times 10^6$ | $[3.03 \pm 1.01] \times 10^6$ |
| $n_{warm}$ [cm$^{-3}$] | - | - | $[1.02 \pm 0.04] \times 10^{10}$ | $[8.90 \pm 0.89] \times 10^9$ |
| $\rho_{warm}$ [g cm$^{-3}$] | - | - | $[1.04 \pm 0.04] \times 10^{-14}$ | $[9.05 \pm 0.91] \times 10^{-15}$ |
| $n_{cool}$ [cm$^{-3}$] | - | - | $[4.18 \pm 0.03] \times 10^{12}$ | $[2.69 \pm 0.09] \times 10^{12}$ |
| $\rho_{cool}$ [g cm$^{-3}$] | - | - | $[4.26 \pm 0.03] \times 10^{-12}$ | $[2.74 \pm 0.09] \times 10^{-12}$ |
| $T_{cool}$ [K] | - | - | $10^4$ | $10^4$ |
| $n_{rain}$ [cm$^{-3}$] | - | - | $[6.98 \pm 0.12] \times 10^{11}$ | $[4.35 \pm 0.91] \times 10^{11}$ |
| $\rho_{rain}$ [g cm$^{-3}$] | - | - | $[7.11 \pm 0.18] \times 10^{-13}$ | $[4.43 \pm 0.92] \times 10^{-13}$ |
| $T_{rain}$ [K] | - | - | $[5.9 \pm 1.5] \times 10^4$ | $[6.2 \pm 0.99] \times 10^4$ |
| $N_{strand}$ | - | - | 6 | 6 |
| $R_{strand}$ [g s$^{-1}$] | - | - | $[1.91 \pm 0.02] \times 10^{10}$ | $[1.37 \pm 0.12] \times 10^{10}$ |
| $F_{strand}$ [g cm$^{-2}$ s$^{-1}$] | - | - | $[5.90 \pm 0.07] \times 10^{-6}$ | $[3.37 \pm 0.11] \times 10^{-6}$ |
| $M_{strand}$ [g] | - | - | $[1.03 \pm 0.01] \times 10^{13}$ | $[2.30 \pm 0.21] \times 10^{13}$ |
| $R_{tot}$ [g s$^{-1}$] | $[2.31 \pm 0.01] \times 10^{10}$ | $[8.61 \pm 0.03] \times 10^{10}$ | $[1.15 \pm 0.01] \times 10^{11}$ | $[8.23 \pm 0.74] \times 10^{10}$ |
| $F_{tot}$ [g cm$^{-2}$ s$^{-1}$] | $[1.76 \pm 0.01] \times 10^{-7}$ | $[3.59 \pm 0.08] \times 10^{-7}$ | $[3.54 \pm 0.04] \times 10^{-5}$ | $[2.02 \pm 0.07] \times 10^{-5}$ |
| $M_{tot}$ [g] | $[1.94 \pm 0.01] \times 10^{13}$ | $[5.16 \pm 0.02] \times 10^{13}$ | $[6.19 \pm 0.07] \times 10^{13}$ | $[1.38 \pm 0.12] \times 10^{14}$ |
| $E_k$ [erg] | $[1.44 \pm 0.02] \times 10^{27}$ | $[6.12 \pm 0.05] \times 10^{27}$ | $[1.29 \pm 0.01] \times 10^{28}$ | $[2.52 \pm 0.03] \times 10^{28}$ |
| $E_{th}$ [erg] | $[3.54 \pm 0.01] \times 10^{28}$ | $[9.06 \pm 0.03] \times 10^{28}$ | $[4.57 \pm 0.01] \times 10^{27}$ | $[1.09 \pm 0.06] \times 10^{28}$ |
| $E_{tot}$ [erg] | $[3.68 \pm 0.02] \times 10^{28}$ | $[9.67 \pm 0.03] \times 10^{28}$ | $[1.75 \pm 0.01] \times 10^{28}$ | $[3.61 \pm 0.03] \times 10^{28}$ |

We take the temperature of the warm rain ($T_{warm}$) as the average DEM-weighted temperature:

$$T_{warm} = \overline{T}_{DEM}, \tag{16}$$

calculated using Equation 10.

We find $T_{warm} = [4.09 \pm 0.59] \times 10^6$ K and $[3.03 \pm 1.01] \times 10^6$ K for SH1 and SH2, respectively. The average $EM$ is calculated using Equation 11 and is found to be $[1.52 \pm 0.67] \times 10^{27}$ cm$^{-5}$ for SH1 and $[1.29 \pm 0.38] \times 10^{27}$ cm$^{-5}$ for
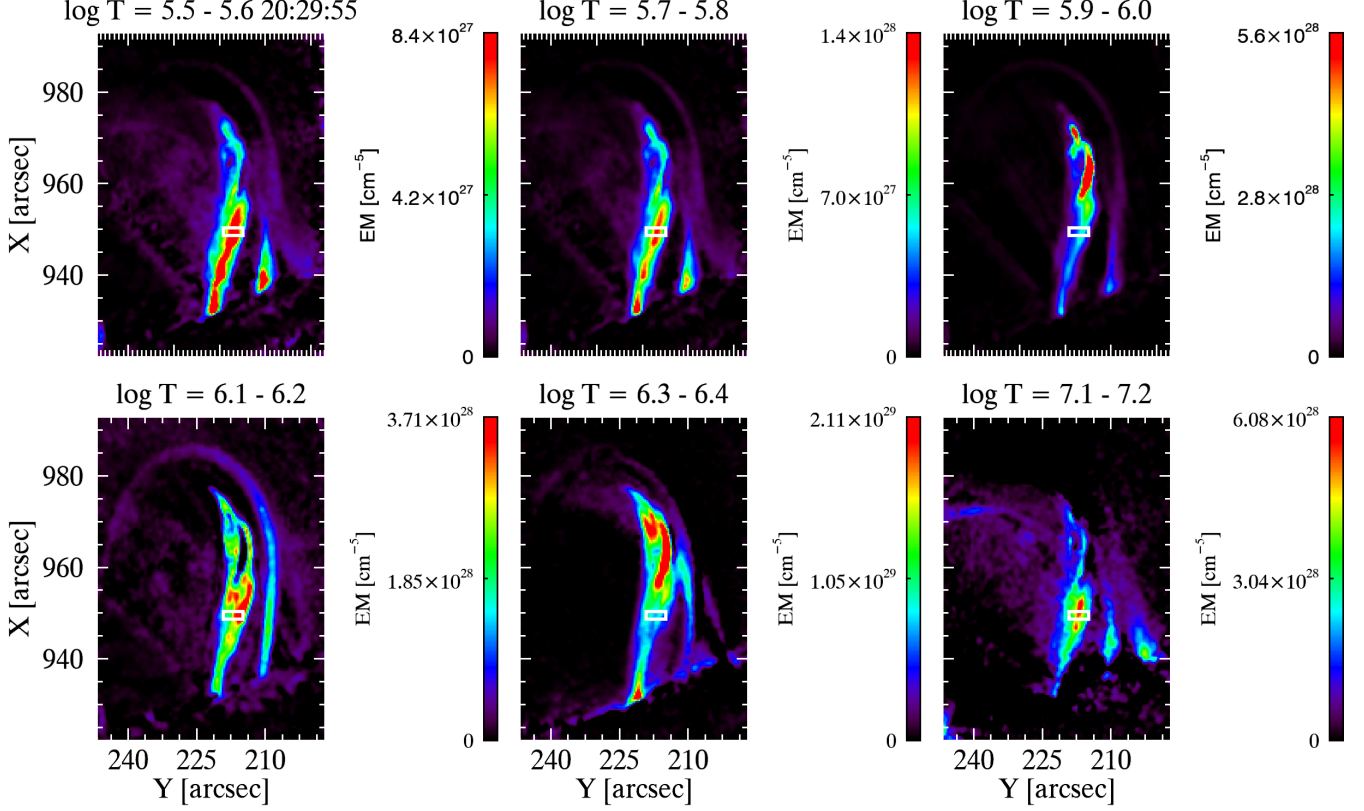
**Figure 23.** *EM* maps for some temperature bins indicated in the title. The white rectangle areas show the focused region within the SH1 for the detailed mass-flux analysis.

SH2. The number density and mass density of the warm plasma is calculated using a similar equation as for the CE:

$$n_{DEM} = \sqrt{\frac{1.2 \times EM}{w_{strand}}}$$

$$n_{warm} = 1.92 n_{DEM} \tag{17}$$

$$\rho_{warm} = 1.17 n_{DEM} m_p,$$

where instead of the overall width, we have now taken the strand width $w_{strand}$, since we are able to resolve the rain strands. As previously mentioned, the thinnest rain strand width is found to be $[642 \pm 56]$ km for the SH1 and $[720 \pm 145]$ km for the SH2, which we take as representatives of the basic (fundamental) structures that form the rain showers.

In order to obtain the total number density ($n_{rain}$) and mass density ($\rho_{rain}$) of the cool part of the rain, we assume that the cool and warm parts of the rain are in pressure balance ($p_{rain} = p_{cool} = p_{warm}$), and also that there is only a small magnetic field variation across the rain (Antolin et al. 2022). The temperature of the cool rain ($T_{cool}$) is taken as the representative temperature value of the SJI 2796 line ($10^4$ K).Then, we have:

$$T_{cool} = 10^4 \text{ K}$$

$$\rho_{cool} = \frac{\rho_{warm} T_{warm}}{T_{cool}} \tag{18}$$

$$n_{cool} = \frac{\rho_{cool}}{0.61 m_p}$$

Similarly to Equation 12, we have assumed a 10% helium abundance in Equation 18. We estimate the volume occupied by the cool part of the rain ($V_{cool}$) with Equation 19, based on the thinnest rain strand observed and the
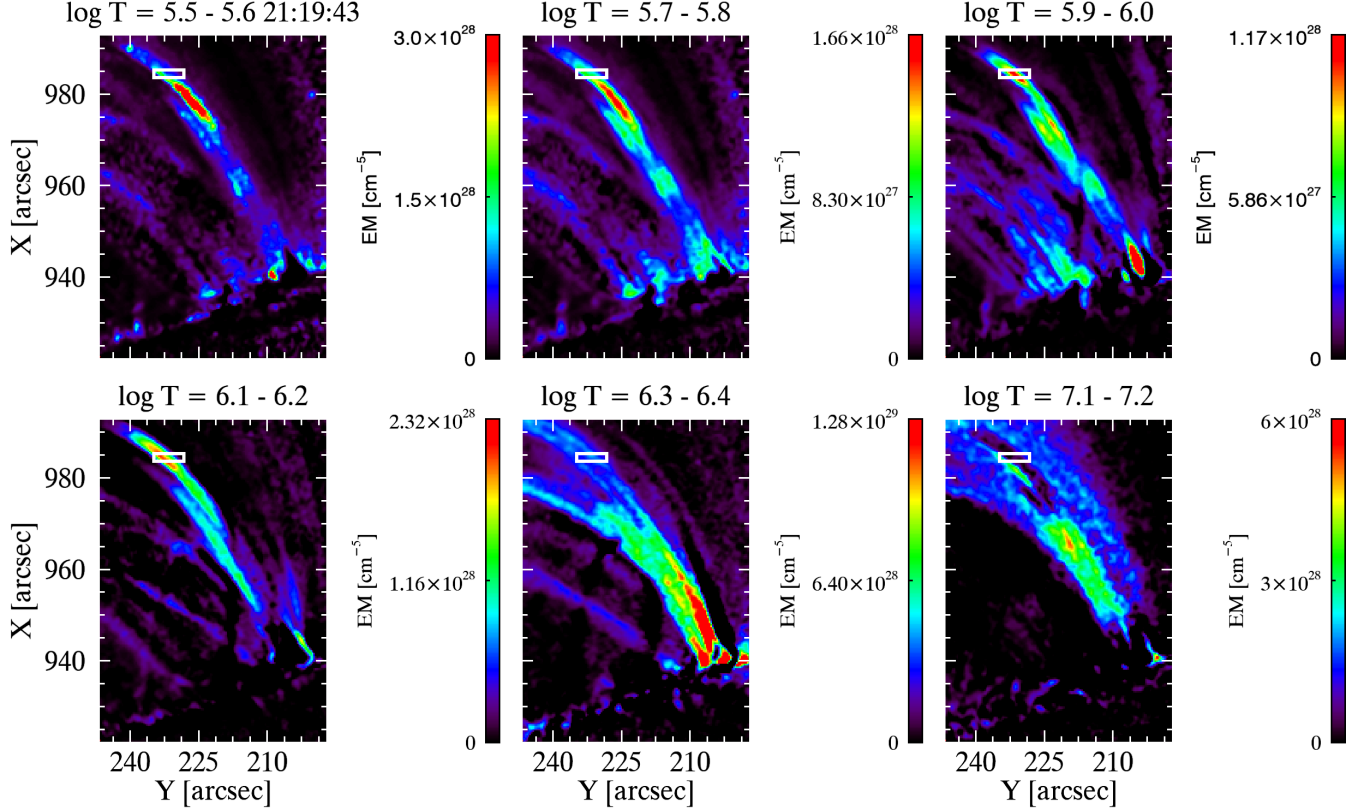
**Figure 24.** Same as Figure 23 but for SH2.

minimum number of such strands ($N_{strand}$) needed to cover the SH width in the POS, which we find to be roughly $N_{strand} = 6$ for both SH1 and SH2.

$$V_{cool} = N_{strand} \times \pi \left( \frac{w_{strand}}{2} \right)^2 v_{tot} \Delta t$$

$$V_{warm} = V_{shower} - V_{cool} \tag{19}$$

Respectively for SH1 and SH2, we find volumes for the cool part of the rain ($V_{cool}$) of $[8.70 \pm 0.14] \times 10^{25}$ cm³ and $[3.12 \pm 1.96] \times 10^{26}$ cm³, and shower volumes ($V_{shower}$) of $[5.28 \pm 2.10] \times 10^{26}$ cm³ and $[1.96 \pm 0.32] \times 10^{27}$ cm³. In an alternative approach, the volume $V_{cool}$ in Equation 19 can be calculated using the RHT results as:

$$V_{cool}^{RHT} = N_t A_{pixel} w_{strand}, \tag{20}$$

where $N_t$ is the total number of rain pixels, $A_{pixel}$ is the area of a pixel and where we have assumed that the emitting plasma along the LOS has a thickness equal to the strand width $w_{strand}$. This approach results in a volume $9.21 \times 10^{25}$ cm³, which is roughly the same as that found with Equation 19.

Since we know the volume occupied by the shower ($V_{shower}$), we can then find the volume of the warm rain ($V_{warm}$), the overall total number density ($n_{rain}$), mass density ($\rho_{rain}$) and temperature ($T_{rain}$) of the rain:

$$n_{rain} = \frac{(n_{cool} V_{cool} + n_{warm} V_{warm})}{V_{shower}}$$

$$\rho_{rain} = 0.61 n_{rain} m_p \tag{21}$$

$$T_{rain} = \frac{p_{rain}}{k_B n_{rain}}.$$

Respectively for SH1 and SH2, we find coronal rain number densities ($n_{rain}$) of $[6.98 \pm 0.12] \times 10^{11}$ cm$^{-3}$ and $[4.35 \pm 0.91] \times 10^{11}$ cm$^{-3}$, and mass densities ($\rho_{rain}$) of $[7.11 \pm 0.18] \times 10^{-13}$ g cm$^{-3}$ and $[4.43 \pm 0.92] \times 10^{-13}$ g cm$^{-3}$. Finally, we find the rain temperatures ($T_{rain}$) of $5.90 \pm 1.50 \times 10^4$ K and $6.20 \pm 0.99 \times 10^4$ K.

Taking $v_{tot}$ as the total rain velocity previously estimated, Equation 13 gives the mass rate ($R_{strand}$) and the mass flux ($F_{strand}$) as $[1.91 \pm 0.02] \times 10^{10}$ g s$^{-1}$ and $[5.90 \pm 0.07] \times 10^{-6}$ g cm$^{-2}$ s$^{-1}$, respectively, per strand for the SH1. For the SH2, these are found to be $[1.37 \pm 0.12] \times 10^{10}$ g s$^{-1}$ and $[3.37 \pm 0.11] \times 10^{-6}$ g cm$^{-2}$ s$^{-1}$ per strand, respectively. Given the duration ($\Delta t$) of 9 min for the SH1 and 28 min for the SH2 over all temperature bins from $\log T = 5.5$ to $\log T = 7.2$, the mass per strand (i.e. $M_{strand} = R_{strand} \times \Delta t$) is found to be $[1.03 \pm 0.01] \times 10^{13}$ g for the SH1 and $[2.30 \pm 0.21] \times 10^{13}$ g for the SH2. To calculate the respective quantities for the entire SH, we multiply by the minimum number of rain strands ($N_{strand}$). Then, we find that the total mass rate ($R_{tot}$) is $[1.15 \pm 0.01] \times 10^{11}$ g s$^{-1}$ for the SH1 and $[8.23 \pm 0.74] \times 10^{10}$ g s$^{-1}$ for the SH2. Finally, we find that a total mass $M_{tot} = [6.19 \pm 0.07] \times 10^{13}$ g and $[1.38 \pm 0.12] \times 10^{14}$ g goes down in SH1 and SH2, respectively.

The kinetic energy ($Ek$) of the SH events is given by Equation 14, with $\rho = \rho_{rain}$ and $V = V_{shower}$. We find $E_k = [1.29 \pm 0.01] \times 10^{28}$ erg and $[2.52 \pm 0.03] \times 10^{28}$ erg, respectively, for SH1 and SH2.

We also calculated the thermal energy of the showers using the Equation 15, with $n = n_{cool}$, $T = T_{cool}$ and $V = V_{shower}$[2], resulting in $[4.57 \pm 0.01] \times 10^{27}$ erg for the SH1 and $[1.09 \pm 0.06] \times 10^{28}$ erg for the SH2. Consequently, the total energies for the SH1 and SH2 are $[1.75 \pm 0.01] \times 10^{28}$ erg and $[3.61 \pm 0.03] \times 10^{28}$ erg, respectively. A summary of all these calculations is given in Table 5.

Since we obtained density parameters for the flare-driven, we would also like to compare them with their quiescent counterpart. For this, we selected a few clumps from the pre-flare phase and obtained average $EM$ and density measurements using the same equations above. The average $EM$ for the quiescent rain is found to be $[1.60 \pm 0.45] \times 10^{26}$ cm$^{-5}$, which is an order of magnitude lower than that of the flare-driven coronal rain. The average mass density of the warm quiescent rain ($\rho_{warm}$) is $[3.38 \pm 0.13] \times 10^{-15}$ g cm$^{-3}$. Then, the average total number ($n_{rain}$) and mass densities ($\rho_{rain}$) of quiescent coronal rain are $[9.01 \pm 0.70] \times 10^{10}$ cm$^{-3}$ and $[9.18 \pm 0.71] \times 10^{-14}$ g cm$^{-3}$, respectively, indicating that the flare-driven rain is $\approx 6$ times denser than the quiescent coronal rain.

## 5. DISCUSSION AND CONCLUSIONS

In this paper, we present a detailed investigation of the mass and energy flow during a C2.1-class flare, whose start and end are marked by the chromospheric evaporation and coronal rain, respectively. We determine their morphology, mass and energy, and compare the values between the observed inflow into the flaring loop and outflow from the loop. We further present a statistical comparison between the quiescent (pre-flare) and flare-driven coronal rain (gradual).

We have checked the rain quantity and rain intensity in the pre-flare and gradual phases. We found that the rain quantity increases by a factor of 3.09, 6.15, and 3.89 times from pre-flare to gradual phase for the SJI 2796 Å, SJI 1330 Å, and Cool AIA 304 Å, respectively. Similarly, the rain intensity also increases by a factor of 3.14, 2.95, and 4.35 for the SJI 2796 Å, SJI 1330 Å, and Cool AIA 304 Å, respectively, from pre-flare to gradual phases. On the other hand, the average mass density of coronal rain increases by a factor of 6.28 from pre-flare to the gradual phases. This strong increase in density is not reflected by the strong increase in intensity, which may reflect the transition to optically thick radiation of the flare-driven rain. The net increase in rain quantity in terms of area from pre-flare to gradual phase in the SJI 2796 Å, 1330 Å, and Cool AIA 304 Å is comparable, with the range of $[5.26, 5.92] \times 10^{12}$ km$^2$ across all channels. This similarity suggests that the plasma is continuously cooling all the way down to the SJI 2796 Å temperatures. The similar trend across the channels also suggests a very fast cooling in the $10^4 - 10^5$ K range, with basically no appreciable time difference in the intensity peaks. Furthermore, this also suggests that very little material stays at $10^5$ K temperatures. However, if everything cools to the SJI 2796 Å temperature formation and nothing remains at higher temperatures, a decrease in the amount of rain in the SJI 1330 Å and Cool AIA 304 Å channels would be observed. This suggests that there is a mechanism, such as the CCTR (Antolin 2020), that guarantees strong co-located emission in time and space at hotter temperatures even if there is continuous catastrophic cooling all the way down to the SJI 2796 Å.

We have also investigated the morphology of these two types of coronal rain. We found that the width of rain clumps varies from 0.2 Mm to 2 Mm with roughly 0.7 Mm (for the SJI channels) and 1.2 Mm (for the AIA channel) on average in both pre-flare and gradual phases. These results are in agreement with the current literature in terms of quiescent

---

[2] Note that because the pressure of the cool and warm rain material is the same, it is equivalent to take $n = n_{warm}$ and $T = T_{warm}$ in Equation 15.

coronal rain studies (such as Antolin et al. 2015; Li et al. 2022; Şahin et al. 2023). In this study, we have also included flare-driven coronal rain morphology and on average, there is basically no change in the width from pre-flare to gradual phases, with only a maximum increase of 10% (for the SJI 2796 Å), which can be explained based on the amount of rain increase in the POS, leading to more LOS superposition of structures. Furthermore, for both the pre-flare and gradual phases, the width of the rain clumps remains fairly uniform as they fall along the loop, suggesting that the factor influencing rain width is unaffected by the varying thermodynamic conditions with height (e.g. progressive cooling or increased compression downstream from the rain). All these results highlight the fundamental and consistent nature of rain widths largely independent of the physical quantities that vary strongly during the flare or with height, such as the field strength, densities and temperatures. This largely invariant nature of the rain widths reflects a more fundamental mechanism setting the widths (contrary to the lengths). An early study by van der Linden & Goossens (1991) demonstrated that the widths could be set by the eigenfunction of the thermal mode, which suggests that rain widths reflect the detailed evolution of the instability of this MHD wave. A recent 2.5D MHD numerical simulation by Antolin et al. (2022) showed the emergence of a fundamental magnetic field strand generated from TI due to gas pressure loss and flux freezing, suggesting that total pressure balance across the field may define the rain width. This is further supported by the recent 3D MHD numerical modelling from Ruan et al. (2024), where the Lorentz force and the pressure gradient closely balance each other across the flare loop during its evolution. This means that we can use pressure equilibrium purely between the gas pressure in the flare loop $p_{gas}$ and the surrounding magnetic pressure to calculate the average magnetic field strength ($B$) during the impulsive and gradual phases, as $\frac{B^2}{8\pi} = p_{gas}$. Taking the thermodynamic values for each case (see Table 5), we obtain a magnetic field strength of 23.78 G and 10.92 G for the impulsive and gradual phases, respectively, which are consistent with the numerical results of Ruan et al. (2024) for a similar C-class flare. The decrease in field strength, which translates into a magnetic total energy of $\approx 3.71 \times 10^{29}$ erg, is consistent with the calculated total thermal energy of the flare ($7.52 \times 10^{29}$ erg). DKIST, with the capability of measuring the coronal magnetic field strength, should be able to directly assess these theoretical assumptions.

Contrary to the clump widths, the clump lengths vary from a few Mm to 22 Mm. We found that the average length of flare-driven coronal rain is 1.50, 1.54, and 1.20 times larger than the pre-flare quiescent coronal rain. This can be simply explained by the large increase in rain quantity, with the growth largely occurring along the field for a given clump (while the rain width stays constant). Contrary to the invariance of the rain widths with height, the lengths of rain clumps increase at lower heights up to a threshold set by the falling time of the rain, the length of the loop, and the inability of the RHT method to follow the clumps on disk.

We then examined the rain dynamics during the pre-flare and gradual phases and found that both types of rain exhibit a wide range of velocities spanning from a few km s$^{-1}$ to 200 km s$^{-1}$. These results are in agreement with the previous numerical (Fang et al. 2015a; Li et al. 2022) and observational (Antolin & Rouppe van der Voort 2012; Şahin et al. 2023) studies. Rain clumps do not only move downward but also upward and in varying trajectories. The occurrence of the upward motions and the change in the trajectory of rain clump is first noted by Antolin et al. (2010). Recent studies (Li et al. 2022; Şahin et al. 2023) have shown how ubiquitous these upward motions of coronal rain are in the solar atmosphere. Şahin et al. (2023) found that upflow velocities can have higher values than downflow velocities. However, these upflow motions correspond to more stochastic and sporadic motions. In other words, contrary to downward motions, upward motions are more localised events and do not correspond to bulk flows. Our findings showed that downflow velocity values are increased by a factor of 1.40 from the pre-flare to the gradual phase, with minimal variation observed across the channels. The upflow speeds show negligible to little increase from pre-flare to gradual phases (with a maximum factor of 1.25 for SJI 1330 Å). We have also examined the average projected velocity in relation to both downward and upward motions as a function of height. At higher heights, we observe downward accelerations in both pre-flare and gradual phases. However, the rain maintains a consistently steady speed during its falling, potentially owing to a combination of effective gravity and pressure variations (Antolin et al. 2010; Oliver et al. 2014; Martínez-Gómez et al. 2020). In contrast to the downward motion, we observe a more chaotic behaviour in the upward motion concerning the variation in projected velocity with height. The bulk increase in downflow speeds is in agreement with the hydrodynamic effect discussed in Oliver et al. (2014); Martínez-Gómez et al. (2020). It has been shown numerically that, as the mass and density of the clumps increase, the drag due to the gas pressure gradient force leads to an increase in speed given by $v_{max} = 2.56\Theta^{0.64}$ (Martínez-Gómez et al. 2020), where $\Theta = \rho_{rain}/\rho_{DEM}$ is the density ratio between the rain clump and the surrounding region (Martínez-Gómez et al. 2020). In this study, we found that the maximum POS velocity for flare-driven coronal rain ($\approx 70$ km s$^{-1}$ on average at a height of 5 Mm, cf. Fig. 9) is 1.4 times larger than the corresponding maximum velocity for quiescent rain (roughly 50 km s$^{-1}$ on average at a

height of 5 Mm, not shown here). We have also calculated the average total number and mass densities of quiescent and flare-driven coronal rain. For quiescent coronal rain, these values were found to be $[9.01\pm0.70]\times10^{10}$ cm$^{-3}$ and $[9.18\pm0.71]\times10^{-14}$ g cm$^{-3}$, respectively, which are consistent with usual quiescent rain densities Antolin & Froment (2022). For the flare-driven rain, we have found $[5.77\pm0.55]\times10^{-13}$ g cm$^{-3}$ for the mass densities, which constitutes an increase of roughly 6 times the quiescent values. Using the previous results, we can now test the formula by Martínez-Gómez et al. (2020). We can write the formula as follows:

$$\frac{v_{rain,fl}}{v_{rain,qs}} = \left[\left(\frac{\rho_{rain,fl}}{\rho_{rain,qs}}\right)\left(\frac{\rho_{DEM,qs}}{\rho_{DEM,fl}}\right)\right]^{0.64} \tag{22}$$

Here, $v_{rain,fl}$ and $v_{rain,qs}$ correspond to the maximum velocities of flare-driven and quiescent coronal rain, respectively. By taking the density values of the rain ($\rho_{rain}$) and the surrounding area ($\rho_{DEM}$ from outside the rain), we obtain the expected velocity ratio in Equation 22, $\frac{v_{rain,fl}}{v_{rain,qs}} = 1.65$, closely matching the observational result. This supports the theory that gas pressure drag controls the final speed of the rain (Oliver et al. 2014).

A potential explanation for the small increased upflow velocities could be attributed to the appearance of the rain itself. As it falls, cooling occurs, resulting in increased opacity and further rain appearance along the trajectory, which in turn gives rise to the perception of localised, rapid motions depending on the cooling rate. This effect would be particularly visible at the trail of the rain, leading to apparent upflows, and therefore may better explain the localised (and sporadic) behaviour of the upflows. However, it remains unclear whether this effect can fully account for the sporadic nature of the upflows.

We have focused on the impulsive phase and found that the RHT is also able to capture the dynamics of CE. Once again, there are many more CE events; however, we only focused on the best CE events regarding their isolation since it is difficult to analyze all of them due to their diffuse emission. We also analyzed dynamics of both CE events using the CRISPEX/TANAT and found a broad velocity distribution between 15 and 230 km s$^{-1}$, with an average of 125 km s$^{-1}$. A natural question is whether some of the observed upward propagating features correspond to slow magnetoacoustic waves rather than flows. Indeed, it is usually very difficult to distinguish between a wave and a flow (De Moortel et al. 2015). The numerical flare model by Fang et al. (2015b) reveals that initial flow motions in flaring loops are often accompanied by slow-mode waves, with the two phenomena initially appearing indistinguishable. In their numerical model, which includes temperatures similar to those reported in our study, both wave and flow propagate at the same speed, which initially is close to 600 km s$^{-1}$, corresponding to the sound speed for a $10^{7.1}$ K plasma. However, subsequent analysis reveals distinct characteristics of propagating slow modes, including periodic motion and intensity modulation corresponding to reflections at the loop footpoints. In our study, the speeds we observe are significantly lower than the sound speed. Also, we do not observe a modulation of the intensity (which would correspond to the reflection of the slow mode from the far footpoint). Hence, this suggests that the signature we observe is only the flow. Furthermore, the upward propagating features that we interpret as a flow exists over tens of minutes, long enough for a slow mode to propagate back and forth between the loop (and damp, given the very fast damping times usually reported). We were also able to observe the selected CE events in the Fe XXI 1354.08 Å line with the SG spectrometer of *IRIS*, thereby providing a measure for the Doppler and non-thermal velocities, as well as additional support for the flow nature and $10^7$ K temperature of the CEs. Combining the LOS and POS average velocities, we were able to give upper bounds for the total velocities of the CEs. We estimated that the average total upward velocities are $122\pm38$ km s$^{-1}$ and $154\pm33$ km s$^{-1}$ for CE1 and CE2, respectively.

We then presented a comparative study of these two main CE events with two associated SH events. Despite the diffuse emission associated with CE, substructures within it suggest the presence of strands with a minimum width of $1376\pm106$ km on average, seen with both the SJI and SG instruments. The observed minimum sub-structure for the SH events, on the other hand, is $681\pm100$ km on average. Jing et al. (2016) found a strong similarity between the widths of flare ribbons and the widths of rain during an M-class flare, with values in the range of 80-200 km. They interpret their result as a fundamental scale of mass and energy transport during flares. Since CE is directly associated with the flare ribbons, we can compare our results with those of Jing et al. (2016). The CE and rain widths that we find are a factor of $5-10$ larger, which could be attributed to the $5-10$ times coarser spatial resolution (particularly in hot lines) between *GST* and *IRIS*, the diffuse coronal emission (which introduces stronger LOS superposition effects), and the different opacity between H$\alpha$ and the *IRIS* spectral lines. Furthermore, our measurements of the CE widths are performed at (low) coronal heights, and it is likely that the loop area expansion also implies an increase in the width of the CE strands. These factors could also be responsible for the factor of two discrepancy that we find between

the CE and the rain widths. On the other hand, the overall average widths of the CE are found to be $4807 \pm 131$ km with the SJI (matched with SG), which are very similar to the overall average widths of the SHs of $4149 \pm 130$ km. This suggests that spatial resolution and the diffuse coronal emission leading to LOS superposition may be the dominant factors between the factor of two discrepancy. These results align with those of Jing et al. (2016) in that the rain structure can reflect the spatial scales of energy transport during flares. We showed that this association can be further extended to the amount of mass and energy in the evaporated material.

It is important, however, to distinguish the strand widths in CE with those that are found for EUV strands during rain events. As shown in Antolin et al. (2022), the CCTR can strongly emit in the EUV, leading to strands of the same width as the rain. A very recent study by Antolin et al. (2023) with Solar Orbiter/HRIEUV in the 174 Å channel, with the highest resolution ever achieved in the EUV of the solar corona, also showed that the observed rain widths are similar to those of EUV strands. However, they also noted that these EUV strands primarily become evident just before the appearance of rain. This implies that the EUV strand widths may be governed by the cooling mechanism (i.e., TI) rather than the heating length scales. In essence, both heating and cooling length scales can result in similar widths.

The spectral results revealed a significant difference in Doppler and non-thermal velocities between the CEs, suggesting the presence of magnetic shear close to the footpoints of the loop. Furthermore, we found an interesting difference between the dynamics of SH1 and CE1. While CE1 is less Doppler shifted but with a larger non-thermal line width, SH1 is more Doppler shifted (with opposite sign to CE) but with a smaller non-thermal line width, but both SH1 and CE1 have very similar summed Doppler and non-thermal velocities. Given the strong morphological similarity between both, this indicates the presence of unresolved emission and/or turbulence at faster speeds for the CE (supported by the POS measurements with the SJI). With the SG results we were able to properly determine the duration of the CE events. We noticed a rapid decrease in speed on a timescale of $2-5$ min, which suggested a transition from explosive to gentle evaporation. The observed timescales and speeds are consistent with previous reports (Fletcher et al. 2013; Sellers et al. 2022). The decrease in nonthermal velocity for CE2 was not accompanied by a decrease in Doppler velocity, indicating an initially present turbulence that decreases over time (Polito et al. 2019).

Finally, we examined the mass and energy cycle of the flare, where the CE marks the upflow into the flare loop during the impulsive phase, and the SH marks the downflow out of the loop during the gradual phase. Taking an average total number density of $[1.85 \pm 0.02] \times 10^{10}$ cm$^{-3}$ for the CE events, an average overall width of $4807 \pm 131$ km, we obtain an average upflow mass flux for CE events of $[2.67 \pm 0.04] \times 10^{-7}$ g cm$^{-2}$ s$^{-1}$. For the SH events, using the corresponding average values (see Table 5), we found a value of $[2.78 \pm 0.05] \times 10^{-5}$ g cm$^{-2}$ s$^{-1}$. We then estimated the mass going up to be roughly $[3.55 \pm 0.01] \times 10^{13}$ g on average for the CE events. On the other hand, the estimated total mass going down is $[9.99 \pm 0.65] \times 10^{13}$ g on average for the SH events, and is, therefore, roughly three times larger than the mass pushed up. Regarding the energy budget, we found the average kinetic and thermal energies to be $[3.78 \pm 0.03] \times 10^{27}$ erg and $[6.30 \pm 0.02] \times 10^{28}$ erg, respectively, for the CE events. For SH events, we found average kinetic and thermal energies of $[1.90 \pm 0.02] \times 10^{28}$ erg and $[7.73 \pm 0.31] \times 10^{27}$ erg, respectively. In conclusion, the average total energies are $[6.67 \pm 0.02] \times 10^{28}$ erg and $[2.68 \pm 0.02] \times 10^{28}$ erg for the CE and SH events, respectively. This result shows that the rain energy corresponds to roughly half of the CE energy, with the other half probably converted into heat. We note that, in terms of rain energy, only 15 showers would account for the estimated total flare energy. A number of factors can account for the difference in mass between upflow through CE and downflow through SH. First, it is likely that most of the material in the loop is becoming thermally unstable (the loop becomes fully evacuated), with the resulting coronal rain flowing mainly towards the observed footpoint, as seen in AIA 304 Å. Second, it is highly probable that CE occurs at the other footpoint of the loop (which remains beyond the IRIS FOV), and we would expect an additional source for the CE to contribute roughly in equal amounts. Third, it is possible that the CE lasts for longer times but remains undetected. This would be the case if the CE occurs at hotter temperature regimes outside those of AIA and *IRIS*, or remains in a gentle state but is too faint. The next-generation spectrometers, such as *MUSE* (De Pontieu et al. 2022; Cheung et al. 2022) and *EUVST* (Imada et al. 2024), which probe a wider temperature and velocity range at higher sensitivity, will be able to elucidate this problem. These findings support the noteworthy role of coronal rain in the mass and energy exchange between the chromosphere and the corona during a flare.

## APPENDIX

## REFERENCES

Ahn, K., Chae, J., Cho, K.-S., et al. 2014, SoPh, 289, 4117, doi: 10.1007/s11207-014-0559-x

Antiochos, S. K., MacNeice, P. J., Spicer, D. S., & Klimchuk, J. A. 1999, ApJ, 512, 985, doi: 10.1086/306804

Antolin, P. 2020, Plasma Physics and Controlled Fusion, 62, 014016, doi: 10.1088/1361-6587/ab5406

Antolin, P., Auchère, F., Winch, E., Soubrié, E., & Oliver, R. 2024, Living Reviews in Solar Physics, PREPRINT (Version 1) available at Research Square, doi: 10.21203/rs.3.rs-3953676/v1

Antolin, P., & Froment, C. 2022, Frontiers in Astronomy and Space Sciences, 9, doi: 10.3389/fspas.2022.820116

Antolin, P., Martínez-Sykora, J., & Şahin, S. 2022, ApJL, 926, L29, doi: 10.3847/2041-8213/ac51dd

Antolin, P., & Rouppe van der Voort, L. 2012, ApJ, 745, 152, doi: 10.1088/0004-637X/745/2/152

Antolin, P., Shibata, K., & Vissers, G. 2010, ApJ, 716, 154, doi: 10.1088/0004-637X/716/1/154

Antolin, P., Vissers, G., Pereira, T. M. D., Rouppe van der Voort, L., & Scullion, E. 2015, ApJ, 806, 81, doi: 10.1088/0004-637X/806/1/81

Antolin, P., Dolliou, A., Auchère, F., et al. 2023, A&A, 676, A112, doi: 10.1051/0004-6361/202346016

Chen, H., Tian, H., Li, L., et al. 2022, A&A, 659, A107, doi: 10.1051/0004-6361/202142093

Cheung, M. C. M., Martínez-Sykora, J., Testa, P., et al. 2022, ApJ, 926, 53, doi: 10.3847/1538-4357/ac4223

Chitta, L. P., Peter, H., & Young, P. R. 2016, A&A, 587, A20, doi: 10.1051/0004-6361/201527340

Şahin, S., & Antolin, P. 2022, ApJL, 931, L27, doi: 10.3847/2041-8213/ac6fe9

Şahin, S., Antolin, P., Froment, C., & Schad, T. A. 2023, ApJ, 950, 171, doi: 10.3847/1538-4357/acd44b

Culhane, J. L., Vesecky, J. F., & Phillips, K. J. H. 1970, SoPh, 15, 394, doi: 10.1007/BF00151847

De Groof, A., Berghmans, D., van Driel-Gesztelyi, L., & Poedts, S. 2004, A&A, 415, 1141, doi: 10.1051/0004-6361:20034252

De Moortel, I., Antolin, P., & Van Doorsselaere, T. 2015, SoPh, 290, 399, doi: 10.1007/s11207-014-0610-y

De Pontieu, B., Title, A. M., Lemen, J. R., et al. 2014, SoPh, 289, 2733, doi: 10.1007/s11207-014-0485-y

De Pontieu, B., Testa, P., Martínez-Sykora, J., et al. 2022, ApJ, 926, 52, doi: 10.3847/1538-4357/ac4222

Del Zanna, G. 2013, A&A, 558, A73, doi: 10.1051/0004-6361/201321653

Del Zanna, G., Dere, K. P., Young, P. R., & Landi, E. 2021, The Astrophysical Journal, 909, 38, doi: 10.3847/1538-4357/abd8ce

Doschek, G. A., Mariska, J. T., Strong, K. T., et al. 1994, ApJ, 431, 888, doi: 10.1086/174540

Dudík, J., Polito, V., Janvier, M., et al. 2016, ApJ, 823, 41, doi: 10.3847/0004-637X/823/1/41

Fang, X., Xia, C., & Keppens, R. 2013, ApJL, 771, L29, doi: 10.1088/2041-8205/771/2/L29

Fang, X., Xia, C., Keppens, R., & Van Doorsselaere, T. 2015a, ApJ, 807, 142, doi: 10.1088/0004-637X/807/2/142

Fang, X., Yuan, D., Van Doorsselaere, T., Keppens, R., & Xia, C. 2015b, ApJ, 813, 33, doi: 10.1088/0004-637X/813/1/33

Fisher, G. H., Canfield, R. C., & McClymont, A. N. 1985, ApJ, 289, 414, doi: 10.1086/162901

Fletcher, L., Hannah, I. G., Hudson, H. S., & Innes, D. E. 2013, ApJ, 771, 104, doi: 10.1088/0004-637X/771/2/104

Fletcher, L., Dennis, B. R., Hudson, H. S., et al. 2011, SSRv, 159, 19, doi: 10.1007/s11214-010-9701-8

Foukal, P. 1978, ApJ, 223, 1046, doi: 10.1086/156338

Froment, C., Antolin, P., Henriques, V. M. J., Kohutova, P., & Rouppe van der Voort, L. H. M. 2020, A&A, 633, A11, doi: 10.1051/0004-6361/201936717

Golding, T. P., Leenaarts, J., & Carlsson, M. 2017, A&A, 597, A102, doi: 10.1051/0004-6361/201629462

Golub, L., & Pasachoff, J. M. 2009, The Solar Corona

Heinzel, P., & Shibata, K. 2018, ApJ, 859, 143, doi: 10.3847/1538-4357/aabe78
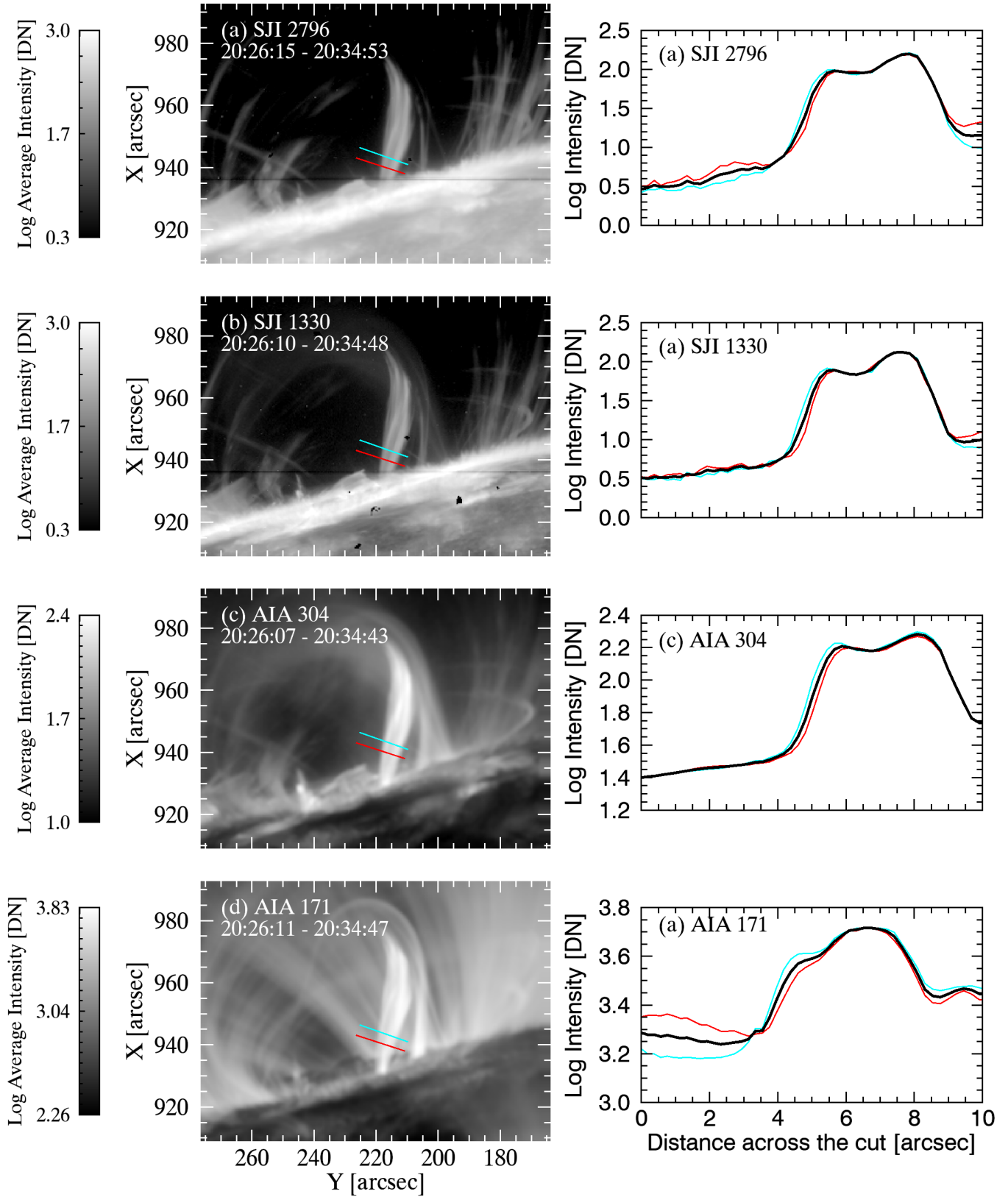
**Figure A.1.** Left: Observed SH1 event during the gradual phase in SJI 2796 Å, SJI 1330 Å, AIA 304 Å, and AIA 171 Å. The red and cyan colours indicate the perpendicular cuts to the loop trajectory. Right: The intensity variation over the distance of these perpendicular cuts. Black curves show the average of these intensity variations.

Hough, P. V. 1962, Method and means for recognizing complex patterns, US Patent 3,069,654

Imada, S., Ugarte-Urra, I., De Pontieu, M., et al. 2024, Submitted to PASJ

Jing, J., Xu, Y., Cao, W., et al. 2016, Scientific Reports, 6, 24319, doi: 10.1038/srep24319

Kleint, L., Antolin, P., Tian, H., et al. 2014, ApJL, 789, L42, doi: 10.1088/2041-8205/789/2/L42

Klimchuk, J. A. 2019, SoPh, 294, 173, doi: 10.1007/s11207-019-1562-z

Klimchuk, J. A., & Luna, M. 2019, ApJ, 884, 68, doi: 10.3847/1538-4357/ab41f4

Kohutova, P., Verwichte, E., & Froment, C. 2019, A&A, 630, A123, doi: 10.1051/0004-6361/201936253

Landi, E., Del Zanna, G., Young, P. R., Dere, K. P., & Mason, H. E. 2012, ApJ, 744, 99, doi: 10.1088/0004-637X/744/2/99

Leenaarts, J., Pereira, T. M. D., Carlsson, M., Uitenbroek, H., & De Pontieu, B. 2013, ApJ, 772, 89, doi: 10.1088/0004-637X/772/2/89

Lemen, J. R., Title, A. M., Akin, D. J., et al. 2012, SoPh, 275, 17, doi: 10.1007/s11207-011-9776-8

Li, L., Zhang, J., Peter, H., et al. 2018, ApJL, 864, L4, doi: 10.3847/2041-8213/aad90a

Li, X., Keppens, R., & Zhou, Y. 2022, ApJ, 926, 216, doi: 10.3847/1538-4357/ac41cd

Liu, W., Antolin, P., & Sun, X. 2016, in AAS/Solar Physics Division Meeting, Vol. 47, AAS/Solar Physics Division Abstracts #47, 4.02

Martínez-Gómez, D., Oliver, R., Khomenko, E., & Collados, M. 2020, A&A, 634, A36, doi: 10.1051/0004-6361/201937078

Mason, E. I., Antiochos, S. K., & Viall, N. M. 2019, ApJL, 874, L33, doi: 10.3847/2041-8213/ab0c5d

Milligan, R. O., & Dennis, B. R. 2009, ApJ, 699, 968, doi: 10.1088/0004-637X/699/2/968

Müller, D. A. N., Hansteen, V. H., & Peter, H. 2003, A&A, 411, 605, doi: 10.1051/0004-6361:20031328

Müller, D. A. N., Peter, H., & Hansteen, V. H. 2004, A&A, 424, 289, doi: 10.1051/0004-6361:20040403

Nelson, C. J., Krishna Prasad, S., & Mathioudakis, M. 2020, A&A, 636, A35, doi: 10.1051/0004-6361/201937357

Oliver, R., Soler, R., Terradas, J., Zaqarashvili, T. V., & Khodachenko, M. L. 2014, ApJ, 784, 21, doi: 10.1088/0004-637X/784/1/21

Pesnell, W. D., Thompson, B. J., & Chamberlin, P. C. 2012, SoPh, 275, 3, doi: 10.1007/s11207-011-9841-3

Plowman, J., & Caspi, A. 2020, ApJ, 905, 17, doi: 10.3847/1538-4357/abc260

Polito, V., Testa, P., & De Pontieu, B. 2019, ApJL, 879, L17, doi: 10.3847/2041-8213/ab290b

Rathore, B., & Carlsson, M. 2015, ApJ, 811, 80, doi: 10.1088/0004-637X/811/2/80

Reep, J. W., Antolin, P., & Bradshaw, S. J. 2020, ApJ, 890, 100, doi: 10.3847/1538-4357/ab6bdc

Ruan, W., Keppens, R., Yan, L., & Antolin, P. 2024, arXiv e-prints, arXiv:2403.19204, doi: 10.48550/arXiv.2403.19204

Schad, T. 2017, SoPh, 292, 132, doi: 10.1007/s11207-017-1153-9

Schad, T. A. 2018, ApJ, 865, 31, doi: 10.3847/1538-4357/aad962

Schad, T. A., Penn, M. J., Lin, H., & Judge, P. G. 2016, ApJ, 833, 5, doi: 10.3847/0004-637X/833/1/5

Schrijver, C. J. 2001, SoPh, 198, 325, doi: 10.1023/A:1005211925515

Scullion, E., Rouppe van der Voort, L., Antolin, P., et al. 2016, ApJ, 833, 184, doi: 10.3847/1538-4357/833/2/184

Sellers, S. G., Milligan, R. O., & McAteer, R. T. J. 2022, ApJ, 936, 85, doi: 10.3847/1538-4357/ac87a9

Shibata, K., & Magara, T. 2011, Living Reviews in Solar Physics, 8, 6, doi: 10.12942/lrsp-2011-6

Sweet, P. A. 1958, in Electromagnetic Phenomena in Cosmical Physics, ed. B. Lehnert, Vol. 6, 123

Testa, P., & Reale, F. 2012, ApJL, 750, L10, doi: 10.1088/2041-8205/750/1/L10

Tian, H., & Chen, N. H. 2018, ApJ, 856, 34, doi: 10.3847/1538-4357/aab15a

Ugarte-Urra, I., & Warren, H. P. 2014, ApJ, 783, 12, doi: 10.1088/0004-637X/783/1/12

van der Linden, R. A. M., & Goossens, M. 1991, SoPh, 134, 247, doi: 10.1007/BF00152647

Vashalomidze, Z., Kukhianidze, V., Zaqarashvili, T. V., et al. 2015, A&A, 577, A136, doi: 10.1051/0004-6361/201424101

Verwichte, E., Antolin, P., Rowlands, G., Kohutova, P., & Neukirch, T. 2017, A&A, 598, A57, doi: 10.1051/0004-6361/201629634

Young, P. R., Tian, H., & Jaeggli, S. 2015, ApJ, 799, 218, doi: 10.1088/0004-637X/799/2/218
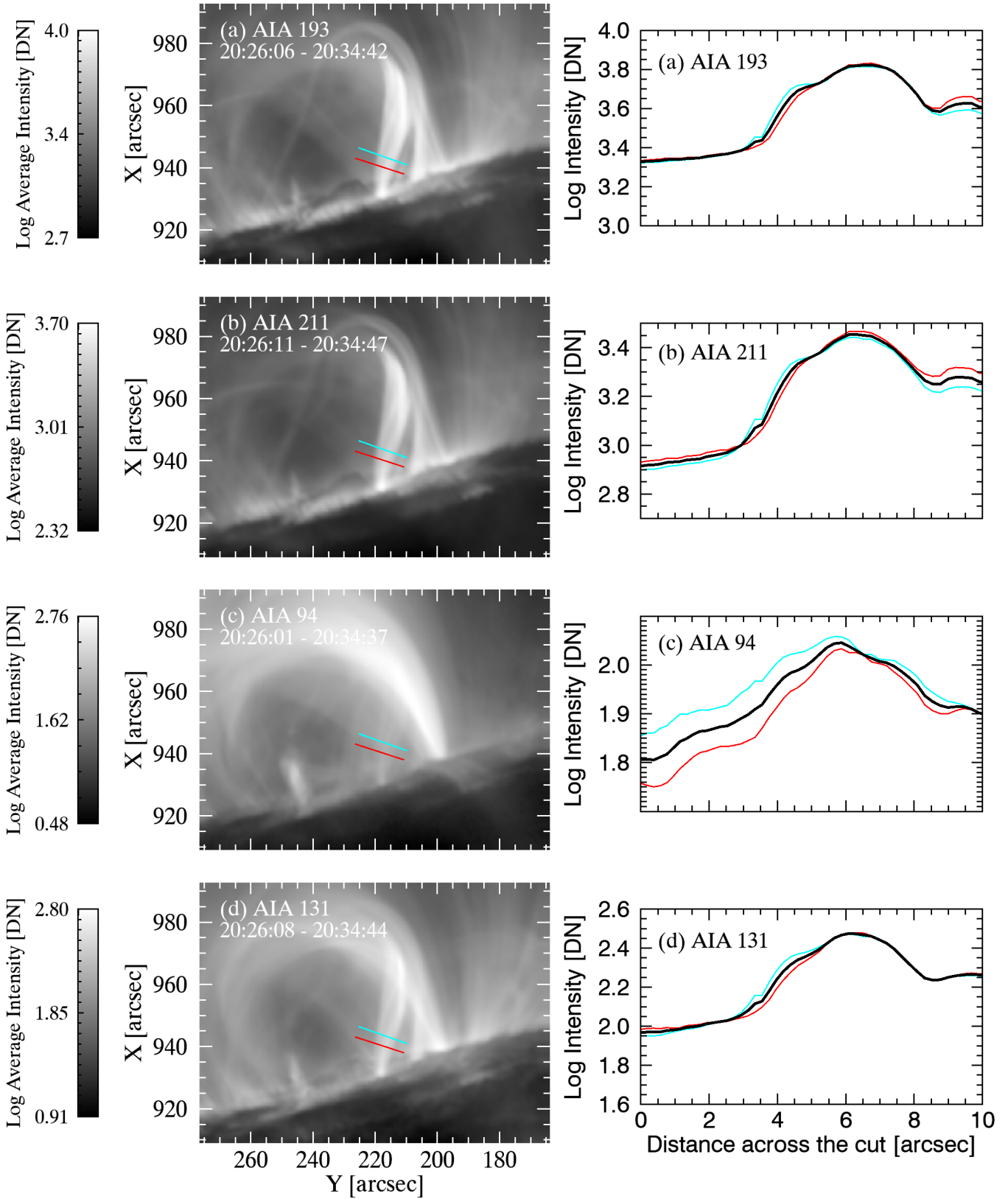
**Figure A.2.** Left: Observed SH1 event during the gradual phase in AIA 193 Å, 211 Å, 94 Å, and 131 Å. The red and cyan colours indicate the perpendicular cuts to the loop trajectory. Right: The intensity variation over the distance of these perpendicular cuts. Black curves show the average of these intensity variations.